Research Paper

3D electrode configurations for spectral induced polarization surveys of landfills

Clemens Moser [a,*], Andrew Binley [b], Adrian Flores Orozco [a]

[a] Research Unit Geophysics, Department of Geodesy and Geoinformation, TU Wien, Vienna, Austria
[b] Lancaster Environment Centre, Lancaster University, Lancaster, UK

ABSTRACT

There is growing interest in the use of spectral induced polarization (SIP) surveys to characterize the near-surface environment. Few attempts have been made to perform field SIP surveys in a 3D configuration; when done, they are typically conducted using a series of parallel 2D electrode lines with collinear measurements. However, such measurements are limited in the resolution between the lines which is critical in the case of heterogeneous subsurface conditions, such as in landfills. To overcome this, we investigate here the enhanced resolution in SIP measurements through true 3D measurements, i.e., the resolving capabilities of different electrode configurations distributed across measuring planes. First, we investigate, through a synthetic study, the difference between results from using 2D parallel collinear electrode arrays and true 3D configurations. Second, we collected SIP data (in the frequency range between 1 and 240 Hz) using 2D and 3D configurations in two landfills to evaluate the application of our results in real field conditions. Both the synthetic and the field experiments demonstrate that measurements of parallel 2D collinear arrays result in the creation of artifacts and the loss of resolution in the 3D structure, especially of polarizable features. In contrast, the 3D configurations are able to resolve polarizable anomalies in synthetic and field measurements, resulting in a better delineation of the geometry of waste units. Our results also demonstrate that 3D configurations are better suited to recover the frequency-dependence of the electrical properties; thus, permitting an improved interpretation of waste composition and the quantification of waste volume.

1. Introduction

The spectral induced polarization (SIP) imaging method is an extension of the electrical resistivity tomography (ERT) and provides not only variations in the electrical resistivity (as commonly obtained by means of ERT) but also resolves variations in the induced polarization, which quantifies the accumulation of charges at the electrical double layer (EDL) formed at the interface between pore water and the grain interface. Such polarization response is strongly dependent on the content of metallic minerals (see Pelton et al., 1978) as well as the surface charge and surface area of the grains (see Binley and Slater, 2020 and references therein). Measurements are collected at different frequencies, typically in the range between 0.001 and 1000 Hz, to gain information about the frequency-dependence of the electrical properties (for an overview see e.g., Kemna et al., 2012; Binley and Slater, 2020). Several studies have revealed the sensitivity of SIP measurements to soil textural parameters (e.g., Revil et al., 2017; Weller et al., 2010), geochemical properties (e.g., Slater et al., 2007; Flores-Orozco et al., 2020) and hydrogeological properties (e.g., Binley et al., 2005; Weller et al., 2015; Revil et al., 2021; Römhild et al., 2022). Built on such links, field investigations have demonstrated the potential of the SIP method in

environmental investigations, such as the understanding of the driving forces of landslides (Revil et al., 2020; Flores Orozco et al., 2022; Gallistl et al., 2022), as well as the distribution and transport of groundwater contaminants (e.g., Cassiani et al., 2009; Flores Orozco et al., 2012a; Slater et al., 2010; Bording et al., 2019). There is also growing interest on the application of the SIP method at the field scale to understand geochemical and microbially-mediated processes in the subsurface (Atekwana and Atekwana, 2010; Flores Orozco et al., 2011; McAnallen et al., 2018; Katona et al., 2021). Due to its sensitivity to the geometrical and chemical properties of the pore-space, the SIP method offers great potential for investigating waste compositions in landfills.

Geophysically-based approaches to investigate the internal state of landfills typically combine direct methods (i.e., chemical analysis of gas, waste and leachate samples) and geophysical measurements (for a review see Nguyen et al., 2018). ERT has become a well-established geophysical method for the delineation of the landfill geometry (Chambers et al., 2006; Soupios et al., 2007; Maurya et al., 2017; Di Maio et al., 2018) and the identification of leachate plumes (Clément et al., 2010; De Carlo et al., 2013; Bichet et al., 2016), which are commonly conductive due to a high salinity (Frid et al., 2017; Maurya et al., 2017). However, materials with negligible surface charge or water

---

content are both related to high resistivity values, for instance in case of dry waste as well as construction and demolition waste (CDW) and thus, hindering the identification of landfill composition using investigations only based on resistivity measurements (Leroux et al., 2007). In some studies, time-domain IP measurements have been used to improve the delineation of organic waste unit(s) in landfills (Johansson et al., 2007; Dahlin et al., 2010; Nguyen et al., 2018), considering the strong contrast between organic waste (commonly associated with a high electrical polarization) and the host geology that may have low polarization characteristics (e.g., Leroux et al., 2007; Frid et al., 2017). Recently, Flores-Orozco et al. (2020) demonstrated the potential of IP to map areas with high methane production in municipal solid waste (MSW) (also referred to as biogeochemically active zones) due to the association with a high polarization. The authors revealed a lineal correlation between the polarization response and the total organic carbon (TOC), which in turn is linked to high methane production.

Gazoty et al. (2012) demonstrated the potential of using the frequency-dependence of the complex conductivity to improve the discrimination of different waste types. However, their study used only 2D measurements collected in the time-domain. To the best of our knowledge, to date no study has reported SIP measurements in landfills: all relevant studies have applied induced polarization (IP) measurements collected at a single-frequency or in the time-domain (e.g., Leroux et al., 2007; Gazoty et al., 2012).

Landfills are highly complex systems, for example in terms of spatial variability in the geometry of waste (e.g., Dahlin et al., 2010), geochemical composition (e.g., Flores Orozco et al., 2021) and water content (e.g., Steiner et al., 2022). Nonetheless, to-date, ERT and SIP investigations in landfills have been conducted through 2D measurements, i.e., with data collected along collinear electrode arrays, with the imaging plane representing electrical variations collected along each line (e.g., Flores-Orozco et al., 2020). To the best of our knowledge, so far, no study has addressed the collection of true 3D SIP data sets on the field scale. In this study, we investigate the resolving capabilities of different 2D and 3D electrode configurations to properly resolve the subsurface electrical properties and their frequency-dependence in SIP surveys. Building on the results, we evaluate the applicability of 3D SIP images for the identification of waste composition and, thus, the quantification of waste volumes in landfills. We aim to answer to the following questions: (1) Can we obtain the same SIP results using several 2D profiles and real 3D configurations? (2) What is the best 3D SIP configuration for landfill investigations? (3) What is the benefit of using SIP measurements over single-frequency or resistivity surveys in landfills? In a first step, we present SIP imaging results of synthetic modeling experiments at a single-frequency aiming at evaluating the spatial reconstruction quality of different 2D and 3D configurations. In a second step, we investigate the influence of 2D and 3D measurements in the recovered frequency-dependence of synthetic data. In a third step, we present results for 3D SIP field data collected in two landfills regarding spatial and frequency-dependence variability. We demonstrate that the geometry and volume of polarizable anomalies and the frequency-dependence of the electrical properties can be resolved more accurately by using true 3D configurations with more than one dipole orientation than measurements collected through parallel 2D electrode lines. The field data were collected on a municipal solid waste (MSW) and a construction and demolition waste (CDW) landfill, corresponding to high and low polarization responses, respectively.

2. Material and methods

2.1. 3D surveys in ERT and SIP imaging

To-date, ERT and SIP investigations in landfills are mainly conducted through 2D measurements. 2D measurements are only recommended in those cases where the subsurface properties are nearly homogeneously distributed perpendicular to the direction of the electrode line (Bentley and Gharibi, 2004; Chambers et al., 2002; Nimmer et al., 2008), which may be challenging for the case of complex geometries such as landfills. Moreover, a main drawback of 2D surveys (ERT or SIP) is the poor sensitivity of the resulting model in the area between the profiles, which might hinder the interpretation of the results (Chambers et al., 2002). Volume calculations, for instance, of anomalous values related to waste, using several 2D measurements may be biased as they require the interpolation of 2D inversion results (e.g., Wainwright et al., 2016; Katona et al., 2021). This issue is especially critical for complex subsurface conditions such as landfills where spatial variations of the electrical properties are expected in all directions. Moreover, in 2D surveys, topographical changes perpendicular to the profile direction are often ignored within the inversion, although they may influence the inversion result, especially in cases of complex terrain (Bièvre et al., 2018).

By using independent 2D electrode lines, mapping extensive areas permits flexibility, e.g., moving electrode positions or entire electrode arrays due to obstacles; they also allow deep investigations (favored by long separation between current and potential dipoles), high spatial resolution (favored by small electrode spacing) as well as the use of simple electrode configurations and minimal computer resources for 2D modeling and inversion. However, the only way to account for heterogeneous electrical properties and strong topographical changes is through three-dimensional modeling and inversion, which is often used in hydrogeological resistivity investigations (e.g., Chambers et al., 2007; Chambers et al., 2012; Auken et al., 2014; Johnson et al., 2015; Wilkinson et al., 2016; Soueid Ahmed et al., 2018). Chambers et al. (2002) demonstrated that three-dimensional modeling and inversion is even more essential for IP surveys. The authors conducted time-domain IP measurements along parallel 2D lines and inverted the data two-dimensionally (merged for quasi-3D model) and three-dimensionally (3D model). Only 3D modeling correctly recovered a polarizable anomaly (metal drum) in the subsurface, while the quasi-3D model revealed images strongly affected by artifacts.

In contrast to 2D measurements, true 3D measurements require extensive field effort (Van Hoorde et al., 2017), can cover only smaller areas by using the same number of electrodes (Dahlin and Bernstone, 1997) and require significantly more computer resources during the processing of the data (e.g., Johnson et al., 2010). When SIP (rather than ERT) measurements are considered, field survey time (for data collection) and computational resources required (for the modeling and inversion) are increased substantially.

In electrical imaging surveys (i.e., ERT, IP and SIP), a 3D model can be resolved through the inversion of a series of parallel 2D collinear arrays but reducing the extra effort during the field work related to true 3D surveys (e.g., Dahlin et al., 2002a; Aizebeokhai and Singh, 2013; Auken et al., 2014; Abdulsamad et al., 2019). Chenq et al. (2019) illustrate the same approach for a series of non-parallel 2D surveys. However, collecting data along 2D collinear arrays limits to resolve structures between the survey lines (Dahlin et al., 2002a; Dahlin and Bernstone 1997; Chambers et al., 2002). To overcome the limitation of 2D collinear arrays, Loke and Barker (1996) proposed the application of rectangular 2D (in plan) electrode arrays to measure in at least one additional direction. In this regard, Chambers et al. (2002) explored the value of orthogonal survey lines (in true 3D and quasi-3D configurations) to delineate the structure of narrow buried walls.

A simple, and true 3D, ERT survey configuration commonly used (e.g., Auken et al., 2014; Johnson et al., 2015; Boyd et al., 2021) consists of parallel lines with measurements splitting the dipoles within two lines, i.e., injecting current along two electrodes of the current line and measuring the potential along two electrodes of a different line. Dahlin and Bernstone (1997) and Van Hoorde et al. (2017) developed a 3D roll along system consisting of several parallel 2D lines with measurements between every possible line pair (crossline), where one line is used for current injection and one line for potential measurements. Brunner et al. (1999) distributed 72 electrodes along three concentric lines (with a

radius of 200, 400 and 875 m), permitting the use of many dipole orientations, to investigate a deep maar (500 m depth of investigation reach). Tsourlos et al. (2014) demonstrated an improved resolution with measurements collected over parallel concentric lines for the characterization of a tumulus, whereby the lines were set symmetrically around the tumulus. Nyquist and Roth (2005) proposed the use of circle-shaped quadrupoles in a configuration of rectangular lines. Although the main observations regarding signal-to-noise ratio (S/N) or resolution can be extrapolated from 3D ERT to 3D SIP surveys, variations in the signal strength of polarization measurements and particular sources of error (e.g., electrode polarization and electromagnetic coupling) need to be taken into account for the design of 3D SIP measurements. While several studies have shown the advantages of 3D surveys over 2D surveys for resistivity (i.e., ERT) investigations, only Chambers et al. (2002) demonstrated that 3D modeling improves the reconstruction quality of a polarizable anomaly over 2D modeling.

2.2. The spectral induced polarization method

The SIP method is an extension of the resistivity method, which provides a measure of the electrical conductivity and capacitive properties of the subsurface and their frequency-dependence (Binley and Slater, 2020). The method is based on a 4-electrode array where two electrodes are used to inject current, while two additional electrodes measure the resulting electric voltage. SIP measurements can be conducted in the time- or frequency-domain. Time-domain IP (TDIP) measurements consist of a transfer resistance and an integral chargeability (based on sampling of the secondary voltage after switching off the applied current). Analysis of the voltage decay provides some, albeit limited, information about frequency-dependence of electrical properties. In contrast, frequency-domain SIP (FD-SIP) measurements are conducted at different frequencies (f) in the range between 0.001 and 1000 Hz. Measurements at each frequency provide a transfer impedance ($Z^*(f)$) in terms of the magnitude $|Z^*(f)|$ (given by the voltage to current ratio) and the phase-shift between voltage and current ($\varphi(f)$):

$$Z^*(f) = |Z^*(f)|e^{i\varphi(f)} \qquad (1)$$

Inversion of hundreds to thousands of measurements with different 4-electrode combinations results in the distribution of the frequency-dependent complex conductivity ($\sigma^*(f)$). The in-phase, or real component (conductivity, $\sigma'(f)$) describes the conductive properties (energy loss), while the quadrature, or imaginary component (polarization, $\sigma''(f)$) represents the capacitive properties (energy storage). The complex conductivity can also be expressed in terms of its magnitude ($|\sigma^*(f)|$) and its phase ($\varphi(f)$):

$$\sigma^*(f) = \sigma'(f) + i\sigma''(f) = |\sigma^*(f)|e^{i\varphi(f)} \qquad (2)$$

Alternatively, the complex conductivity can be represented by its inverse, the complex resistivity ($\rho^*(f) = 1/\sigma^*(f)$). The low conductivity phase angles measured in geophysical applications (typically below 0.1 rad) (e.g., Binley and Slater, 2020) result in conductivity magnitude values being approximately equal to the in-phase conductivity ($\sigma'(f)$). Note that we adopt throughout the complex conductivity convention for phase angle $\varphi(f)$, i.e., a positive value implies a capacitive effect and is used as an indirect measurement of polarization (valid if $\sigma'(f)$ does not vary strongly with the frequency) along this manuscript, considering that the spectra from $\sigma''(f)$ and $\varphi(f)$ are consistent (Kemna et al., 2004) (for a review of the method see Binley and Slater, 2020 and references therein).

Current conduction in the subsurface can be caused by three mechanisms: (1) the matrix conduction (σ_m) through solid materials, which is negligible in the absence of electrical conductors and semi-conductors such as metals and metallic minerals; (2) the electrolytic conduction (σ_f) through fluid-filled pores; (3) and the frequency-dependent surface conduction ($\sigma_s'(f)$) along the electrical double layer (EDL) formed at the interface between particles and pore water (Binley and Slater, 2020).

$$\sigma'(f) = \sigma_m + \sigma_f + \sigma_s'(f) \qquad (3)$$

The electrolytic conduction mechanism is controlled by the fluid conductivity (σ_w), the pore space geometry and porewater saturation (S_w) (Binley and Slater, 2020; Schurr, 1964; Waxman and Smits, 1968). The strongest polarization response is related to the presence of electrically conducting materials where charges polarize in the EDL as well as within electrical conductors, due to the so-called electrode polarization mechanism (Wong, 1979; Buecker et al., 2018). In the absence of electrical conductors, the strength of the polarization is lower than in the case of electrode polarization and is only related to the surface area and the surface charge of particles (Vinegar and Waxman, 1984; Leroy et al., 2008; Revil and Florsch, 2010; Bücker et al., 2019).

The frequency-dependence in the complex conductivity is commonly analyzed using different relaxation models, the most common being the adaptation by Pelton et al. (1978) of the Cole Cole (CC) model, which can be written in terms of the conductivity:

$$\sigma^* = \sigma_\infty\left(1 - \frac{M}{1 + (i\omega\tau)^c}\right) \qquad (4)$$

where M is the chargeability (dimensionless), defined as $M = (\sigma_\infty - \sigma_0)/\sigma_\infty$. σ_∞ and σ_0 represent the conductivity at high frequency and low frequency respectively. $i = \sqrt{-1}$ is the imaginary number, ω is the angular frequency ($\omega = 2\pi f$), τ represents the relaxation time as the inverse of the critical frequency f_{crit} ($\tau = 1/2\pi f_{crit}$) and c (dimensionless) describes the broadness of the spectrum. Such a phenomenological model lacks a mechanistic link to physical properties of materials and is not adequate in case that the signatures reveal more than one phase maximum (e.g., Nordsiek and Weller, 2008). However, it represents the simplest expression to describe the SIP response characterized by a dispersion model around the critical frequency (at which the maximum conductivity phase value is observed).

SIP measurements are sensitive to errors arising from polarization of the electrodes (when an electrode is used for voltage readings immediately after being used for current injection) as well as electromagnetic coupling related to cross-talk between the cables (Flores Orozco et al., 2021). To minimize the effect of cross-talk some studies have proposed the use of coaxial cables (e.g., Flores Orozco et al., 2021; Maierhofer et al., 2022); whereas others have proposed an alternative approach considering the separation of cables and electrodes used for current injection and potential measurements (Dahlin and Leroux, 2012).

2.3. Modeling/inversion algorithm

In this study, we invert independently every data set collected at different frequencies from the SIP survey. For the forward modeling and the inversion of the data we used the ResIPy code (Blanchy et al., 2020; Boyd et al., 2019), which calls the cR3t 3D complex resistivity inversion code (for details in the algorithm, we refer to Binley and Slater, 2020). cR3t is finite element based, allowing discretization of the domain on a structured or unstructured mesh. The inversion algorithm iteratively solves for the distribution of the complex conductivity, at a given acquisition frequency, in terms of the magnitude ($|\sigma^*|$) and the phase (φ) from a data set given in terms of the electrical impedance (more details in Binley and Kemna, 2005). The iterative procedure continues until the model describes the data to a satisfactory level. cR3t uses a weighted least squares measure of data misfit, which can be expressed as a root mean square misfit (RMS). The RMS is equal to one if the model describes the data satisfactorily (Binley and Slater, 2020).

As a criterion for reliability of the complex conductivity inverse model we use the cumulative sensitivity S, which is the diagonal component of $J^T W^T W J$, where W is the data weight matrix and J is the Jacobian matrix (for more details see: Binley and Slater, 2020). cR3t computes the complex resistivity model for a single-frequency. Repeated

inversion over multiple frequencies provides the frequency-dependence for each parameter cell, which can then be analyzed to determine relaxation model parameters for each cell. We inverted the multi-frequency data independently with two different initial models, a homogenous and a heterogeneous initial model. The latter corresponds to the resistivity inverse model of the lowest frequency and was used to improve the stability of the resolved frequency-dependence. To fit Cole Cole parameters, we used the algorithm implemented by Ruecker et al. (2017) within the pyGIMLi libraries.

2.4. 3D synthetic experiment & configurations

The best way to evaluate an electrode configuration is to quantify the deviation between the resolved (i.e., after the inversion) 3D model and the actual 3D model of the subsurface. Field measurements are not suited for such evaluation as the exact distribution of resistivity values is unknown. To overcome this, we can conduct numerical studies, which are based on a synthetic model (i.e., a given variation of the electrical conductivity in an imaging plane) and use it for the forward modeling of resistances, which in a second step are used for the inversion. In this regard, the difference between the true and inverted model quantifies the reconstruction capabilities of our electrode configuration.

2.4.1. 3D synthetic model

In the SIP synthetic model (see Fig. 1) we defined three regions. Region 1 corresponds to an asymmetrically shaped conductive layer (50 mS/m) with a pit-shape in the central area and a low polarization at 1 Hz ($\varphi = 5$ mrad). The chargeability is low ($M = 0.1$), and the critical frequency is high ($f_{crit} = 75$ Hz). The width of the pit is 24 m on the bottom and 34 m on the top of the pit and the border of the pit has a slope of 45°. Region 2 is a relatively resistive (10 mS/m) layer with a thickness of 3–5 m, depending on the direction, and with the same phase angle, chargeability and critical frequency as in region 1. In the northern and western part, the layer has a depth of 3 m, while the depth in the southern and eastern part is 5 m. In the pit in the center of the model, we embedded a cuboid polarizable anomaly (region 3) with a phase of 30 mrad. The region is resistive, with the same magnitude as in region 2 (10 mS/m), chargeable ($M = 0.4$) and the critical frequency of the region is low ($f_{crit} = 0.5$ Hz). The broadness of the spectra is equal for regions 1–3 ($c = 0.3$). The SIP measurements were simulated in a frequency range of 0.1–240 Hz.

2.4.2. Configurations

We simulated FDIP measurements (magnitude and phase of the transfer impedance) of four different configurations with 64 electrodes

per configuration (see Fig. 2). In configuration *A*, we used single line measurements along two parallel straight lines with a separation of 20 between them, 32 electrodes each and an electrode spacing of 2.5 m (see Fig. 2a). Configuration *B* is based on four parallel lines with a separation of 10 m between them, each line with 16 electrodes with a spacing of 5 m (see Fig. 2b).

Configuration *C* and *D* represent true 3D measurements with more than one dipole direction. Configuration *C* is a grid array with 8 by 8 electrodes set in a rectangular grid with an electrode separation of 5 m in each direction. The electrodes are separated in two chains with 32 electrodes on each chain (see Fig. 2c). Configuration *D* is a circular array with electrodes set in four concentric circles with 7, 13, 19 and 24 electrodes, 5 m electrode separation within each circumference and circle radii of 5.575, 10.350, 15.125 and 19.100 m to keep a fair distribution of electrodes over the entire area of investigation (see Fig. 2d). The lines are set in a circular shape to increase the number of dipole orientations in the measurements, which is defined by the angle of a vector connecting both electrodes of a current or voltage dipole. Similar to configuration *C* line 1 and line 2 are physically separated lines, which are used to separate the current line from the potential line. We placed one electrode at the center of the circumferences (see Fig. 2d) to increase the sensitivity within that area. For the multi-frequency analysis, we simulated measurements with configurations *B* (representing 2D parallel lines) and *C* (representing true 3D measurements).

For the simulation of measurements, we used a dipole–dipole (DD) schedule, with a dipole length of once the electrode spacing (i.e., skip-0, using common notation). Following the forward modeling, we perturbed the computed 'measurements' with an error of 2% (impedance magnitude) and 1 mrad (impedance phase angle) for each configuration. In the inversion, we assumed a relative error of 2% and 2 mrad. We used a higher phase angle error in the inversion than in the forward modeling because when using an absolute phase error of 1 mrad in the inversion we observed slight overfitting in the results. Before inverting the simulated measurements, we removed quadrupoles with an infinite geometric factor (due to crossing voltage/current dipole direction in the center of the current/voltage dipole), as well as those forward measurements associated with a negative phase angle (as noted before, positive phase angles imply a capacitive effect). Synthetic studies permit to quantify the deviations in the inverse model from the real values (defined by the synthetic), in our study we use the normalized root-median-square-error (NRMSE) in % defined as:

$$NRMSE = \frac{\sqrt{median((\boldsymbol{x_{real}} - \boldsymbol{x_{inv}})^2)}}{\overline{x_{real,inv}}} \cdot 100 \qquad (5)$$

Synthetic model

Regions & electrical properties

① $|\sigma^*| = 50$ mS/m, $\varphi = 5$ mrad, $M = 0.1$, $f_{crit} = 75$ Hz, $c = 0.3$

② $|\sigma^*| = 10$ mS/m, $\varphi = 5$ mrad, $M = 0.1$, $f_{crit} = 75$ Hz, $c = 0.3$

③ $|\sigma^*| = 10$ mS/m, $\varphi = 30$ mrad, $M = 0.4$, $f_{crit} = 0.5$ Hz, $c = 0.3$
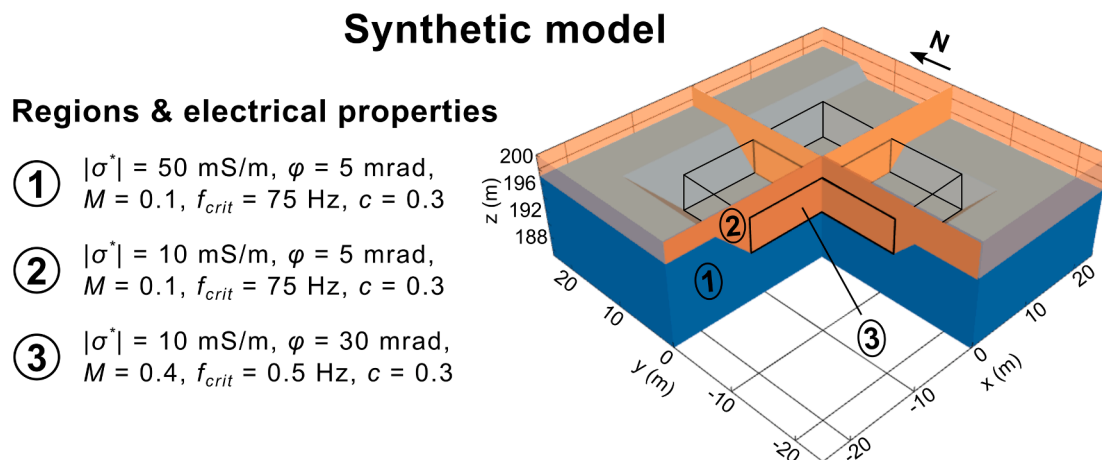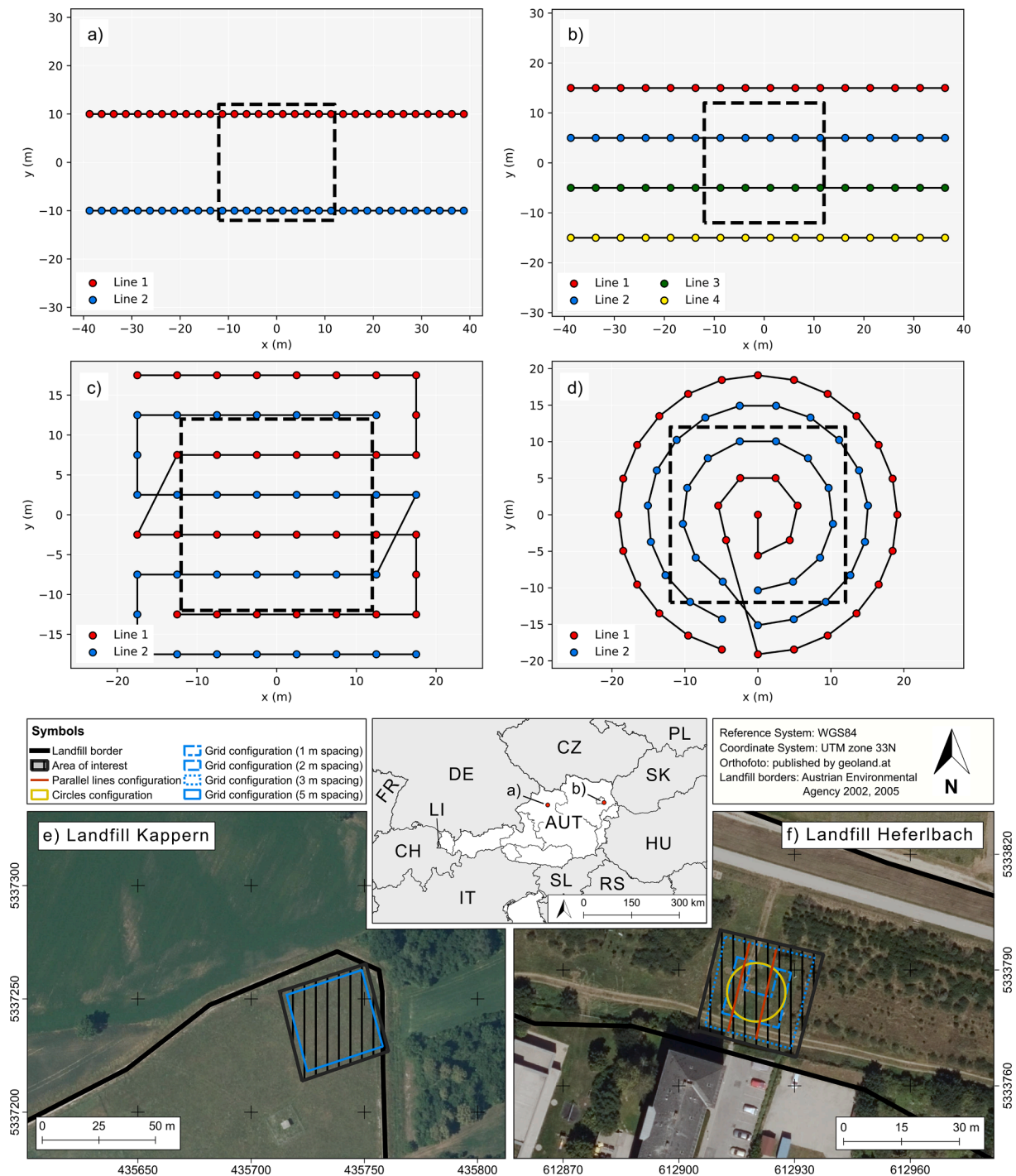
Fig. 1. Model used in the synthetic study for SIP measurement simulations. The SIP model consists of three regions (1–3) with different electrical properties and Cole Cole parameters (given on the left-hand side). At 1 Hz the conductivity magnitude is two-layered with a polarizable anomaly (characterized by high φ values but no changes in $|\sigma^*|$) in the upper layer.

Fig. 2. The electrode configurations investigated (a to d) and location of the (e) Kappern and (f) Heferlbach landfills. Configuration *A* (a) and *B* (b) consist of two/four parallel lines, while configuration *C* (c) is represented by a grid of 8 by 8 electrodes connected by two separated lines, which are hairpin bended. Configuration *D* (d) has four concentric lines with a line distance of 5 m approximately and an electrode separation of 5 m exactly and an additional electrode at the center to increase the sensitivity of the measurement in that position. Measurements at the Kappern landfill (e) were conducted with configuration *C* in the north-east part of the landfill. At the Heferlbach landfill (f) data were collected with configurations *A*, *C* and *D* in a north-west area of the landfill.

where x_{real} are the voxel values (voxels correspond to mesh elements) of the real model, x_{inv} are the voxel values of the inverse model and $x_{\overline{real,inv}}$ corresponds to the average of the voxel values of the real and inverse model.

2.5. Field measurements

2.5.1. Site 1 (landfill Heferlbach) – MSW and high polarization response

The landfill Heferlbach is located southeast of Vienna, Austria, in an oxbow lake of the river Danube (48° 8′ 50.3″ N 16° 31′ 5.2″ E) (see Fig. 2b). Between 1965 and 1974 the former riverbed was mainly filled with MSW, but also land excavation material and CDW with a total volume of 240 000 m³ (Austrian Environmental Agency, 2005). The

66 000 m^2 large landfill is situated on an altitude of about 156–157 m asl (above sea level) with a mean waste depth between 3.0 and 4.5 m. Below the waste material there is an aquifer of quaternary gravels on top of a sand layer. The groundwater table is below the bottom of the waste area at approximately 149 m asl. Chemical analyses show a high rate of landfill gas production due to the high content of organic waste. To accelerate the degradation of organic materials and to avoid the migration of landfill gas into neighboring buildings a horizontal aeration pipes system was erected in 2012 (Brandstätter et al., 2020). We decided to conduct 3D SIP field measurements on an area with high content of MSW in the western-center part of the landfill (see Fig. 2b), where extensive information of the landfill is available (Flores-Orozco et al., 2020; Steiner et al., 2022). The host geological material (lower layer) can be characterized by a moderate conductivity (∼30 mS/m), while the top layer is resistive (<10 mS/m). The highly conductive (>100 mS/m) and polarizing (>30 mrad) MSW unit has a thickness of 4 m approximately and is covered by a 0.5–1.0 m thick forest floor organic layer. More detailed information about the landfill can be found in Austrian Environmental Agency (2005), Brandstätter et al. (2020), Flores-Orozco et al. (2020) and Steiner et al. (2022).

2.5.2. Site 2 (landfill Kappern) – CDW and low polarization response

The landfill Kappern is located in Upper Austria, Austria, (48° 11′ 4.0″ N 14° 08′ 4.8″ E) (see Fig. 2a) on an altitude of 292.5 m asl in a former gravel pit, which was filled with MSW, CDW as well as industrial waste from 1974 to 1983 (Austrian Environmental Agency, 2002). The waste masses extend a volume of 120 000–150 000 m^3 on an area of 30 000 m^2 and are on top of quaternary gravels of the nearby river Traun. The bottom of the landfill is in a depth of 3.5–5.5 m and is not lined. Prior to 1998, leachate percolated into the groundwater body due to the high elevation of the groundwater table (288 m asl). Therefore, a sealing wall surrounding the main part of the landfill was built and the groundwater table was lowered below the landfill bottom, which prevented further potential groundwater pollution. To close the landfill on top the area was covered by multiple layers (about 2 m thick), including a layer of CDW, a gas drainage layer, a fleece, a geotextile, and a vegetated layer (Austrian Environmental Agency, 2002). Until now, there has been no study examining possible landfill gas emissions, and, compared to the Heferlbach landfill, minimal chemical analysis studying the composition and distribution of waste.

2.5.3. SIP field measurements and data processing

In this study, we conducted field-based SIP measurements with the DAS-M (Data Acquisition System Multisource, from MPT-IRIS Inc.), which permits the physical separation of the transmitter and the receiver: the transmitter is connected with a cable array to current electrodes and a second cable array connects the receiver and the voltage electrodes (see LaBrecque et al., 2021). The use of separated lines with physically independent transmitter and receiver with the DAS-M helps to decrease not only the effect of cross-talk between the cables but also within the instrument (Pelton et al., 1978; Dahlin et al., 2002b; Flores Orozco et al., 2021), thus, significantly increasing the quality of the SIP data.

For all measurements, we used 5 m cables and hung them up on plastic tree protections to avoid loops with the cable and reduce sources of electromagnetic coupling. In the case of 2D lines, the separated cables were shifted by one electrode, according to the procedure of Dahlin et al. (2002). As we physically separate the current injection line from the potential measurements line, we used stainless steel electrodes, 64 per configuration (32 electrodes per line), and conducted DD measurements, which provide the most flexible set of quadrupoles for 3D measurements (Chambers et al., 2002). For all field measurements, after injecting current in one line and measuring the potential in the other line, the current and potential lines were changed to provide a reciprocal measurement to each normal measurement (more details about normal-reciprocal pairs see in LaBrecque et al., 1996). At the Heferlbach landfill,

we used configuration A (parallel lines), configuration C (grid array) with electrode separations of 1 m, 2 m and 3 m and configuration D (circular array) (see Table A1 in the supplementary material). At the landfill Kappern we used configuration C with two different skip sizes (i. e., dipole lengths) (see Table A1 in the supplementary material). All measurements were conducted in a frequency range of 1–240 Hz.

The field data were processed in three steps. (1) We calculated the geometric factors based on synthetically modeled transfer resistances of a homogeneous subsurface and removed field measurements where the polarity is inconsistent with the simulated data. (2) The data were independently filtered for each frequency based on the statistical analysis of the relative and absolute normal reciprocal misfit (LaBrecque et al., 1996; Slater et al., 2000; Flores Orozco et al., 2012b). (3) In the case of SIP analyses, quadrupoles, which were removed during the previous processing steps at least in one frequency, were removed in all frequencies to maintain the same quadrupoles for each frequency.

The inversions of all frequencies were started independently under consideration of a relative magnitude and an absolute phase error, which were estimated by the normal reciprocal misfit of the filtered data (e.g., Flores Orozco et al., 2012b). While for the relative magnitude error a constant value for all frequencies was used, the absolute phase error varies with the frequency. At the Heferlbach landfill, for configuration C, a relative magnitude error of 10% was used for all frequencies, while the absolute impedance phase error was 10 mrad for a frequency of 1 Hz (range of impedance phase shift data: 0–85 mrad). For higher frequencies we used the same relative magnitude error but the error for the impedance phase was up to 50 mrad in the case of 240 Hz (range of phase shift readings: 20–200 mrad). Used error values for all configurations are presented in Table A2 in the supplementary material. All inversions resulted in a root mean square (RMS) misfit of about 1. For the inversion of the data, 3D unstructured tetrahedral meshes incorporating the local topography were built with Gmsh (Geuzaine and Remacle, 2009). Fine tetrahedron elements were created around the electrodes, with coarser elements with increasing distance from the electrode positions. The mesh was extended far beyond the survey area to account for 'infinite' current paths. All inversions presented are shown in terms of complex conductivity magnitude $|\sigma*|$ and phase angle φ. In the case of field results, we blanked those cells with a $\log_{10}$ normalized cumulative sensitivity $S_{norm} < -3$ (see Kemna, 2000). The S_{norm} was calculated by the ratio between the cumulative sensitivity S and the 95% quantile of S. The 95% quantile was used because of the large dynamics of sensitivity values (range of S: −7 to 3), particularly close to the surface, although we recognize that such a threshold is somewhat subjective.

3. Results and discussion

3.1. Analysis of spatial resolution in 3D SIP data at 1 Hz

3.1.1. Electrical conductivity imaging results – Conductivity magnitude

The conductivity magnitude $|\sigma*|$ models for all configurations (as observed in Fig. 3) resolve similar spatial structures: (i) a bottom layer with the highest values (25–50 mS/m), and (ii) a top layer with the lowest values (5–20 mS/m). The values for the two layers are in agreement with those defined in the synthetic model, with variations in the range of 18–43% for the top and bottom layer (see Table A3 in the supplementary material). Additionally, Fig. 3 reveals differences in the shape of the interface between the two layers.

Inversion results obtained for configuration A reveal that the interface between the top and bottom layers is correctly resolved below the electrodes (see Fig. 3a), but not in the areas between the electrode lines, where we can observe artifacts or a shallow interface. The NRMSE is slightly higher for the top layer (43%) than for the bottom layer (37%). Configuration B represents a similar electrode geometry but with a shorter separation between the lines and a longer electrode spacing than in configuration A, which improves the imaging results (NRMSE: 23% in
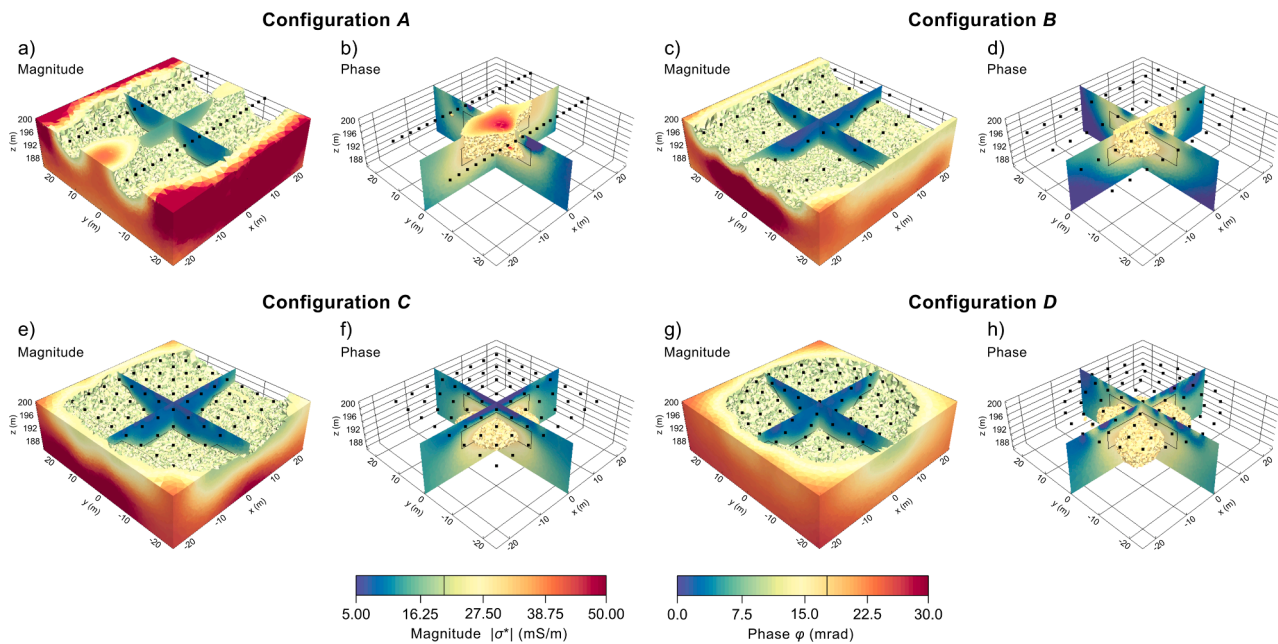
Fig. 3. Inversion results of simulated data of configurations *A–D*. For each configuration the imaging results are given in terms of the conductivity magnitude, $|\sigma^*|$ (a, c, e, g) and phase, φ (b, d, f, h). Both parameters are visualized by two vertical slices, one parallel to the *x*-axis, one parallel to the *y*-axis. Additionally, all mesh elements with $|\sigma^*| > 20$ mS/m in the case of the magnitude and with $\varphi > 17.5$ mrad in the case of the phase are included. Black dots represent the electrodes positions.

top layer and 38% in bottom layer) and avoids the generation of artifacts in the $|\sigma^*|$ images (Fig. 3c) observed in configuration *A*. However, both configurations *A* and *B* have only measurements collected along one direction, which leads to the creation of artifacts in the direction of the electrode lines (i.e., *x*-direction).

Fig. 3e shows that configuration *C* is able to recover correctly the contact between the top and bottom layers. The recovered values in the top layer are more consistent with the true value (19% NRMSE) than in the bottom layer (38% NRMSE) and in average (28%) lower than for configurations *A* (40%) and *B* (30%). However, in the central uppermost area at a depth of <1 m the inversion over-estimates the $|\sigma^*|$ values with maximum difference between true and inverse model above 50%.

As observed in Fig. 3g, the inversion of data using configuration *D* correctly resolves the geometry of the two layers, including the interface between them. However, the corners of the rectangular pit are poorly recovered, likely due to the lack of electrodes located exactly on top of the edges of the anomaly. The $|\sigma^*|$ values are fairly well recovered for the two layers (22% and 43% NRMSE between inverse and real model for the top and bottom layer, respectively), but there are weak patterns of artifacts parallel to the circular electrode lines. Additionally, the shape of the interface between the top and bottom layer is not correctly resolved in the central area related to the low sensitivity of the measuring configuration in this area.

3.1.2. Polarization imaging results – Conductivity phase

In contrast to the conductivity magnitude results discussed above, there are large differences in the structures resolved in the conductivity phase φ imaging results for data collected with the different configurations tested. Inversion results for configuration *A* solved a polarizable anomaly in the center of the study area, but with an incorrect shape when compared to the true model (see Fig. 3b). Particularly, the upper boundary of the anomaly was not resolved by configuration *A* leading to the highest NRMSE value observed (69%) outside the anomaly. As observed in Fig. 3d, the imaging results obtained with configuration *B* are closer to the real (i.e., synthetic) model than those obtained with the configuration *A*, not only regarding the absolute values of the polarizable anomaly (58% NRMSE) but also regarding the geometry of the

interface between the anomaly and the surrounding material. However, the φ values are not correctly resolved between the electrode lines creating artifacts between the electrode lines.

The φ images obtained for configuration *C* resolve for a similar geometry to that of the true model. The shape of the polarizable anomaly is well recovered, but the depth of the lower interface between the anomaly and the surrounding material is not correctly resolved. The position of the anomaly could be accurately determined in the *x*- and *y*-direction but the values are underestimated (61% NRMSE). Additionally, in near-surface areas (1–2 m depth) we can observe an over-shooting of the values down to −5 mrad. Such underestimation of values in the anomaly together with over-shooting outside of the anomaly is likely due to the use of a smoothing term in the regularization, as discussed by Binley and Slater (2020).

The inversion results computed for configuration *D* reveal an accurate delineation of the position of the polarizable anomaly as well as in the recovered value. However, the geometry of the anomaly is not as accurately resolved as with configuration *C*, particularly in the center of the electrodes close to the surface. To improve the resolution in the central area of the concentric circles, we added more quadrupoles with an electrode in the center of the simulated data, which helped to reduce the creation of artifacts, i.e., results in a lower NRMSE value between resolved and true φ values in the IP anomaly (50% versus 60%), but the shape of the anomaly is not significantly improved. Alternatively, placing two electrodes used as a current or potential dipole in the center of the electrode array could improve the sensitivity.

3.2. Recovering the frequency-dependence – SIP imaging results

Several studies have shown that collecting SIP data at a broad frequency-bandwidth might provide further insights for an improved hydrogeological characterization (in comparison to single-frequency data), or to discriminate between different geochemical status (e.g., Flores Orozco et al., 2011, 2022; Kemna et al., 2012). In particular, the frequency-dependence seems to be related to changes in the textural properties of the subsurface (see Binley et al., 2005; Revil and Florsch, 2010) and, thus may help delineate paths for groundwater flow and

storage. Such information is critical in landfills to predict areas with high production of landfill gas or with possible leakage of leachate to groundwater below the landfill. In this regard, it is important to understand the impact of 2D and 3D investigations in the quality of the resolved frequency-dependence of the complex conductivity.

In Fig. 4, we present the resulting spectra and the Cole Cole fit of the SIP (0.1–240 Hz) inverse models, which were based on numerically simulated data, for configuration *B* (2D configuration) and configuration *C* (3D configuration) (see Fig. 4a and b). We extracted voxel values in two zones: (1) between electrode lines (referred to as *Z1*), and (2) directly below the electrodes (referred to as *Z2*) of configuration *B*. Both zones are in region 3 of the synthetic model (c.f., Fig. 1). Additionally, we estimated the relaxation parameters of the SIP inverse models of *Z1* and *Z2* for configuration *B* and *C* and compared them with the true predefined relaxation parameters.

Fig. 4a and 4b demonstrate that 3D configurations (in this case configuration *C*) provide a higher reconstruction quality than 2D configurations (i.e., configuration *B*) regarding both the spatial variations in the electrical properties as well as their frequency-dependence. Likewise, NRMSE values between the resolved and corresponding Cole Cole fitted $|\sigma*|$ (Fig. 4c, i) and φ (Fig. 4c, ii) are lower for configuration *C* than for configuration *B*. Moreover, in the case of configuration *B* the deviations are higher for areas between the electrode lines (*Z1*), where also the single-frequency analysis demonstrated a vulnerability to the

creation of artifacts. This is clearly associated to the lack of sensitivity in our measurements to the areas between the 2D lines, which also reflects in larger uncertainties for the data inverted (independently) at different frequencies. A poor retrieval of the frequency-dependence results in incorrect estimation of relaxation parameters (e.g., fitting incorrectly Cole Cole models) and, thus, the incorrect estimation of textural or hydrogeological properties (e.g., Revil et al., 2017; Binley et al., 2005).

As observed in Fig. 4c, due to the higher reconstruction quality of spectra by 3D configurations, the resolved relaxation time τ (iii) and the chargeability *M* (iv) can be estimated more accurately with configuration *C* than with configuration *B* with lower absolute differences between the estimated and the true relaxation parameters. Additionally, Fig. 4 reveals that the difference in the reconstruction quality between 2D and 3D configurations is lower for τ than for *M*. Such an observation is in agreement with Weigand et al. (2017), who demonstrated that in 2D imaging the reconstruction quality of the chargeability is strongly related to the sensitivity while the reconstruction quality of τ is not dominated by the sensitivity. Thus, the application of 3D configurations over 2D configurations is particularly important for the estimation of the chargeability, which in turn is key for a quantitative interpretation of waste composition (see Flores-Orozco et al., 2020) and water content (see Steiner et al., 2022).To enhance the consistency in the imaging results for SIP data inverted at different frequencies, we decided to use the same initial model to start the inversion. In this case, we used as an
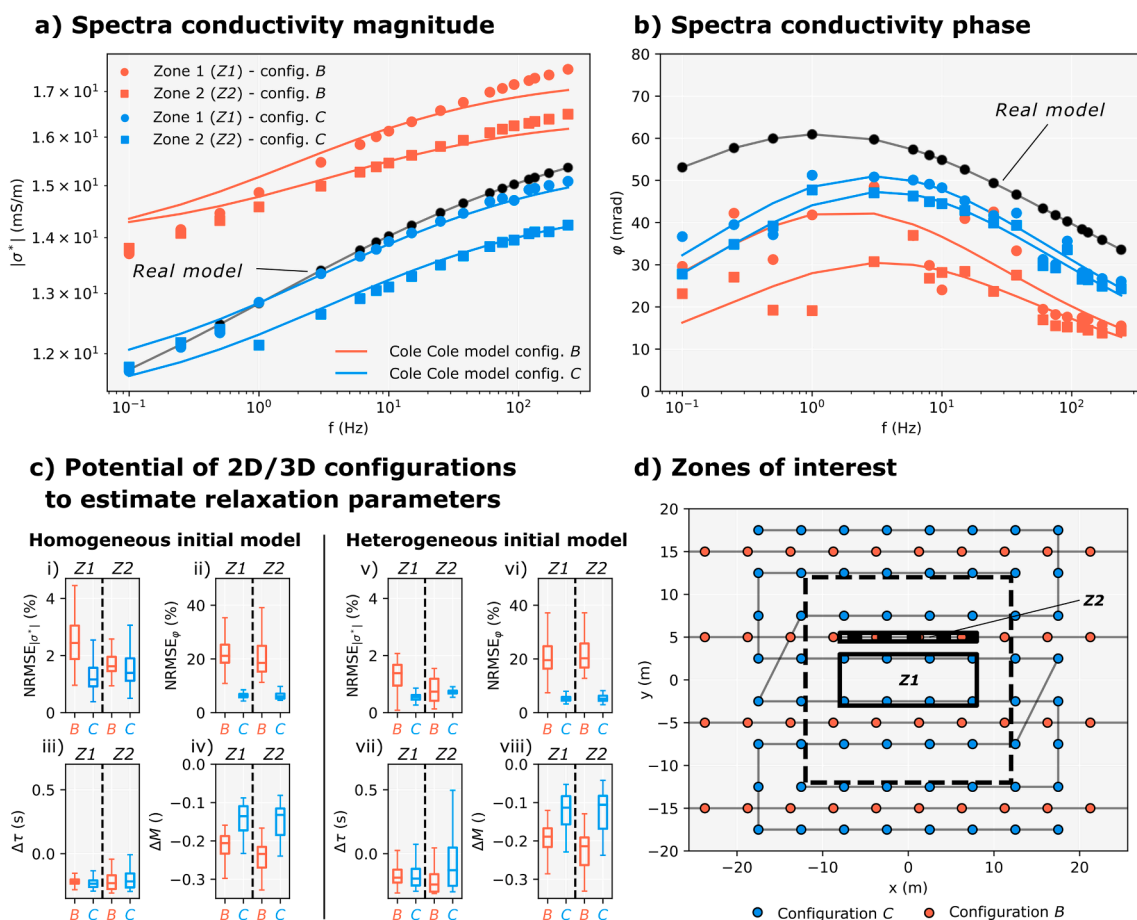
Fig. 4. Analysis of the retrieved Cole Cole parameters (τ and *M*) in the synthetic (numeric) SIP study obtained for configuration *B* (red symbols) and *C* (blue symbols). The complex conductivity spectra for the real and inverted data are presented in terms of the conductivity (a) and phase (b) for the real values and those extracted from the inversion of the data in two voxels of two zones: *Z1* and *Z2* (d). Zone 1 (*Z1*) corresponds to model parameters in the center of the volume of investigation ($x = \pm 8$ m, $y = \pm 3$ m, $z = 193$–197 m), while zone 2 (*Z2*) corresponds to the area below electrodes of configuration *B* ($x = \pm 8$ m, $y = 4.5$–5.5 m, $z = 193$–197 m). Subplots in (c) present the observed discrepancy between the real values of τ and *M* and those obtained after fitting a Cole Cole model to the inversion results obtained for configuration *B* and *C*. Such discrepancy is quantified by means of the NRMSE (subplots i, ii, v, vi) and the absolute difference Δ (subplots iii, iv, vii, viii). We conduct the analysis of the discrepancy in the retrieved Cole Cole parameters for inversions results obtained using a homogeneous (subplots on the left of Fig. 4d) and a heterogeneous (subplots on the right of Fig. 4d) initial model.

initial model those results obtained for the lowest frequency collected (i. e., synthetically simulated). We decided upon the lowest frequency, as field measurements conducted at low frequencies ≤1 Hz are less affected by electromagnetic (EM) coupling (see Flores Orozco et al., 2021). Synthetic studies provide a useful means of evaluating the improvement in the inversion of SIP data by using the same heterogeneous initial model, in comparison to using a homogeneous model. In this regard, subplots (v-vi) show that using the same heterogeneous initial model results in lowering the error values (NRMSE) between the extracted

voxel values and those fitted to the inversion results. The use of a heterogeneous initial model improves the results for both configurations A and C, particularly in the case of the $|\sigma*|$ (v). Considering that the $|\sigma*|$ and φ values are better resolved, the use of a heterogeneous model to start the inversion of SIP data also allows a more accurate estimation of the relaxation parameters τ (vii) and M (viii) with median absolute deviations between estimated and true parameters closer to zero than in the case of a homogeneous initial model.
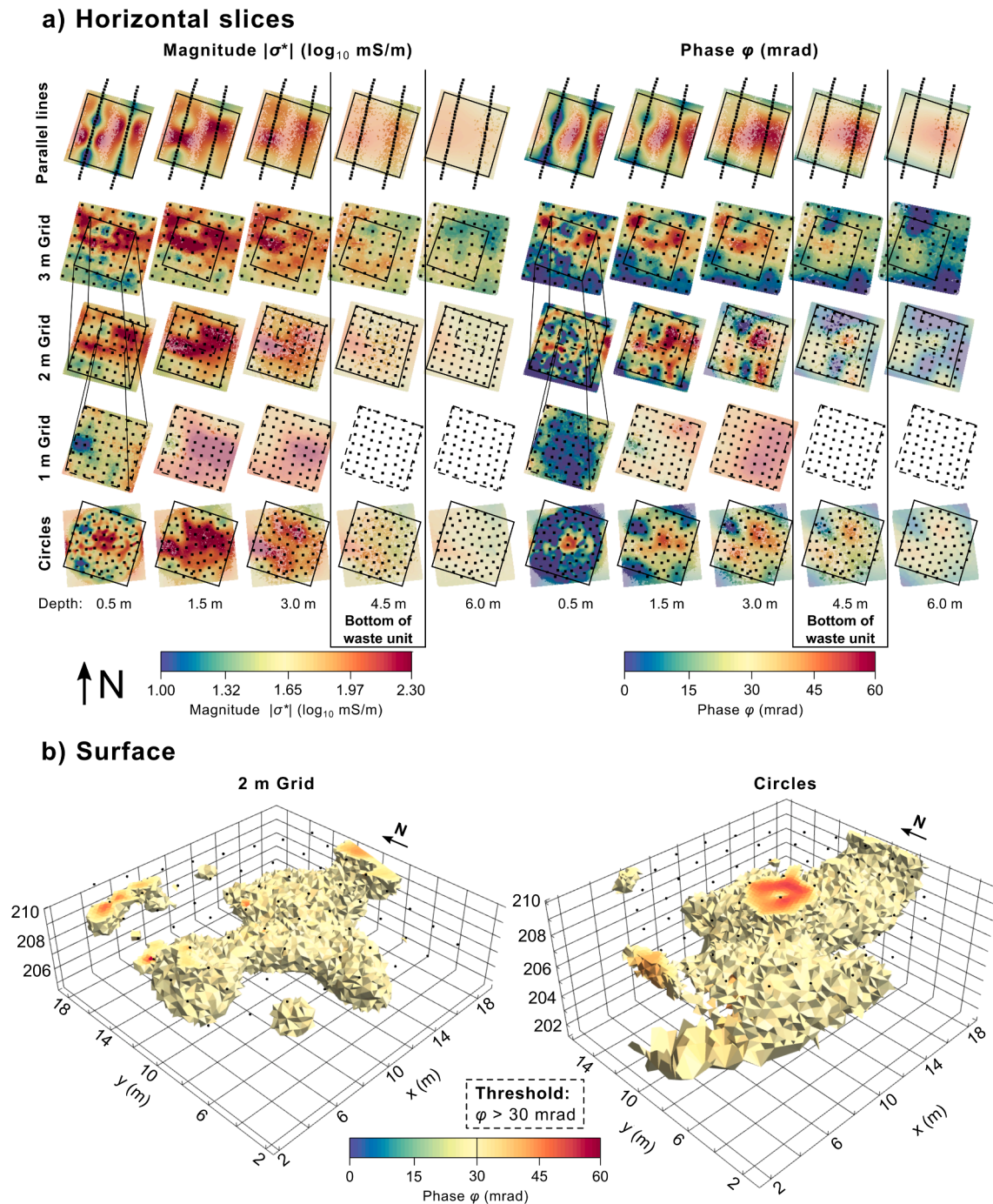

Fig. 5. Imaging results for data collected at the Heferlbach landfill. Horizontal slices (a) of the inversion results for configuration A (line 1), C (line 2–4) and D (line 5) in terms of the magnitude (left) and the phase (right) of the complex conductivity at 1 Hz. For configuration C (line 2–4) the results of the configuration with 3 m, 2 m and 1 m electrode separation are presented. The bottom of the waste unit (according to Flores-Orozco et al., 2020) is indicated by the vertical lines. The solid black rectangle represents the outline of configuration C with 2 m electrode separation, while the dashed black rectangle represents the outline of configuration C with 1 m electrode separation. Additionally, the 3D volumes of the high conductivity phase anomaly ($\varphi \geq 30$ mrads) are presented for configuration C (left) and D (right) obtained at 1 Hz (b). Black dots represent the electrodes positions.

3.3. Evaluating the spatial resolution of 3D measurements at the MSW landfill Heferlbach – Imaging results for data collected at 1 Hz

The imaging results (in terms of $|\sigma^*|$ and φ) at 1 Hz are presented in Fig. 5a as 2D horizontal slices corresponding to the resolved values at depths of 0.5, 1.5, 3.0 and 4.5 m for each configuration. The inversion results of configuration A reveal a high $|\sigma^*|$ and φ anomaly at a depth of 1 to 4 m along both lines and between the lines related to a MSW waste unit (see Flores-Orozco et al., 2020). Similar to the results of the synthetic experiment, in near surface areas (0.5 m) between both electrode lines, the $|\sigma^*|$ and φ values differ dramatically from the values along the electrode lines, which clearly evidence the creation of artifacts due to a lack of sensitivity. Artifacts between the lines can lead to an incorrect interpreted geometry of the anomaly and thus, to a misleading estimation of the waste volume. Such observations are in agreement with resistivity studies from Dahlin et al. (2002) and resistivity and TDIP studies from Chambers et al. (2002). Additionally, this study shows that the resolving capabilities of such 2D configurations are even poorer for IP than for the resistivity (59% NRMSE versus 35% NRMSE), which was also demonstrated, albeit qualitatively, by Chambers et al. (2002).

The results of configuration C collected with different electrode separations (3 m, 2 m and 1 m) presented in Fig. 5a allow to investigate the effect of electrode spacing on the depths of investigation and the maximum resolution for the specific 3D configuration. An electrode spacing of 2 m allows to solve both the upper and lower boundary of the waste unit, which are in a depth of 0.5–1 m and 4.5–5 m respectively, as observed during the collection of samples (see Flores-Orozco et al., 2020 and references therein). As expected, deeper areas can be investigated by the 3 m electrode separation allowing to resolve the lower boundary of the landfill at a depth of ca. 4.5–5 m. However, for the 3 m electrode spacing, the upper boundary of the landfill is not resolved; hence for 3 m spacing the depth of investigation is >4.5 m and the maximum resolution is >1 m. In contrast, imaging results for data collected with 1 m electrode spacing resolve the soil and CDW near to the surface and on the top of the MSW and the boundary to the MSW waste unit within the shallow 2 m depth. Clearly, the data with 1 m electrode spacing are not sensitive to the bottom of the landfill; hence the depth of investigation is <4.5 m and the maximum resolution is <1 m. Based on these observations we propose to use the following rules of thumb to roughly determine the depth of investigation (DOI) and the maximum resolution of the 3D grid array tested: the DOI corresponds to 1/3 of the maximum separation between the current and voltage dipoles $dist_{dip}$ while the maximum resolution of the configuration can be estimated by 1/2 of the electrode spacing $spac_{elec}$.

$$DOI = \frac{1}{3}\max(dist_{dip}) \tag{6}$$

$$Resolution = \frac{1}{2}spac_{elec} \tag{7}$$

Further studies should consider the extension of the proposed experimental model in Equation (6) and (7) to include changes in the conductivity.

Accordingly, Fig. 5a reveals that only configuration C with an electrode separation of 2 m permits the delineation of both the lower and the upper boundary of the landfill. As a result, hereafter, in the case of configuration C, we will only discuss the results obtained with an electrode spacing of 2 m. The inverted data for configuration C delineate two anomalies characterized by the highest $|\sigma^*|$ and φ values (values above 100 mS/m and 30 mrad, respectively). As discussed in detail by Flores-Orozco et al. (2020), these anomalies indicate biogeochemically active zones, associated to the highest methanogenesis in the landfill.

The results of configuration D, presented in Fig. 5a, show the delineation of both the upper and lower boundary of the landfill. Even though the location of the two anomalies is similar to the results of configuration C, the shape of the anomaly is different. Such

discrepancies are likely related to the lack of sensitivity in the center of configuration D as observed in the synthetic study.

In Fig. 5b, we show the φ anomalies as volumes associated with values above 30 mrad, which correspond to the biogeochemical hotspots and might be of particular interest due to their potential for high rates of methanogenesis. The position of the active zones extends to depths between 0.5 m and 4 m approximately and has a volume of 231 m^3 for configuration C and 309 m^3 for configuration D. We do not present such estimation for configuration A as Fig. 5a demonstrates that configuration A is only able to correctly solve the subsurface electrical properties directly below the electrode lines (2D) but not in the volume between the lines (3D).

A key message from this study is the need to perform sensitivity analysis based on numerical experiments prior to carrying out field 3D SIP surveys, to warranty an optimal configuration of electrodes and measurements for the desired depth of investigation and expected main units of the area under investigation. As the synthetic modeling demonstrated, the use of circular arrays does not significantly improve the results in comparison to the grid array, yet the field procedures to set the electrodes in a circular array are more complicated and time-consuming. Additionally, as discussed above, changing the size of configuration C provides clear advantages, as it permits to easily increase the resolution in near-surface areas, the actual extension of the explored area, or the total depth of investigation. Further investigations might also include the inversion of the three different mesh sizes (electrode separation of 1, 2 and 3 m) in a single dataset to quantify a possible improvement in the total area of coverage as well as in the resolution. Hence, for further investigations we recommend the use of a 3D grid array, such as configuration C.

Our study demonstrates the advantages of using true 3D configurations over 2D configurations for numerical as well as for real data. However, applying real 3D configurations on the field can be challenging for example in steep terrain considering the extra effort required at the field scale to define the position of the electrodes, to lay out the cables, connect the electrodes and the device and the higher data acquisition time (see building and data acquisition time for different configurations in Table A1 in the supplementary material). The use of circular configurations is still more challenging as the position of the electrodes cannot be easily defined with measuring tapes. Moreover, mapping of extensive areas may still benefit from simple 2D lines that can be easily relocated at a different position. Nonetheless, for the case of IP measurements, data quality is improved, especially at high frequencies (>1 Hz), when current dipoles are located in a different cable than the one used for voltage readings to minimize cross-talk and other sources of EM coupling (Dahlin and Zhou, Flores Orozco et al., 2021). Hence, 3D mesh configurations, as presented here, offer a great opportunity to gain real 3D data and simultaneously reduce EM coupling quality of the SIP data.

3.4. Resolving the frequency-dependence in 3D SIP imaging results for the MSW landfill Heferlbach

In Fig. 6, we present the results of φ for the frequencies 1, 15 and 75 Hz for 2D and 3D configurations (A and C, respectively) in the Heferlbach landfill. Images of the $|\sigma^*|$ reveal a minimal change for data collected at different frequencies and are in general similar to those presented in Fig. 5a and therefore not presented for the sake of brevity. In contrast, Fig. 6 reveals a significant frequency-dependence in the φ images, which can be further exploited to understand changes in waste composition, for example. For both configurations, φ values decrease from 1 to 15 Hz and increase for higher frequencies (i.e., at 75 Hz). Configuration C resolves a consistent distribution of polarizable anomalies at different frequencies with a high resolution, while configuration A is not able to resolve the anomalies with the same level of detail, particularly for the areas between the electrode lines. The polarization at low frequencies (e.g., 1 Hz and below) is most likely related to the

Configuration *A*
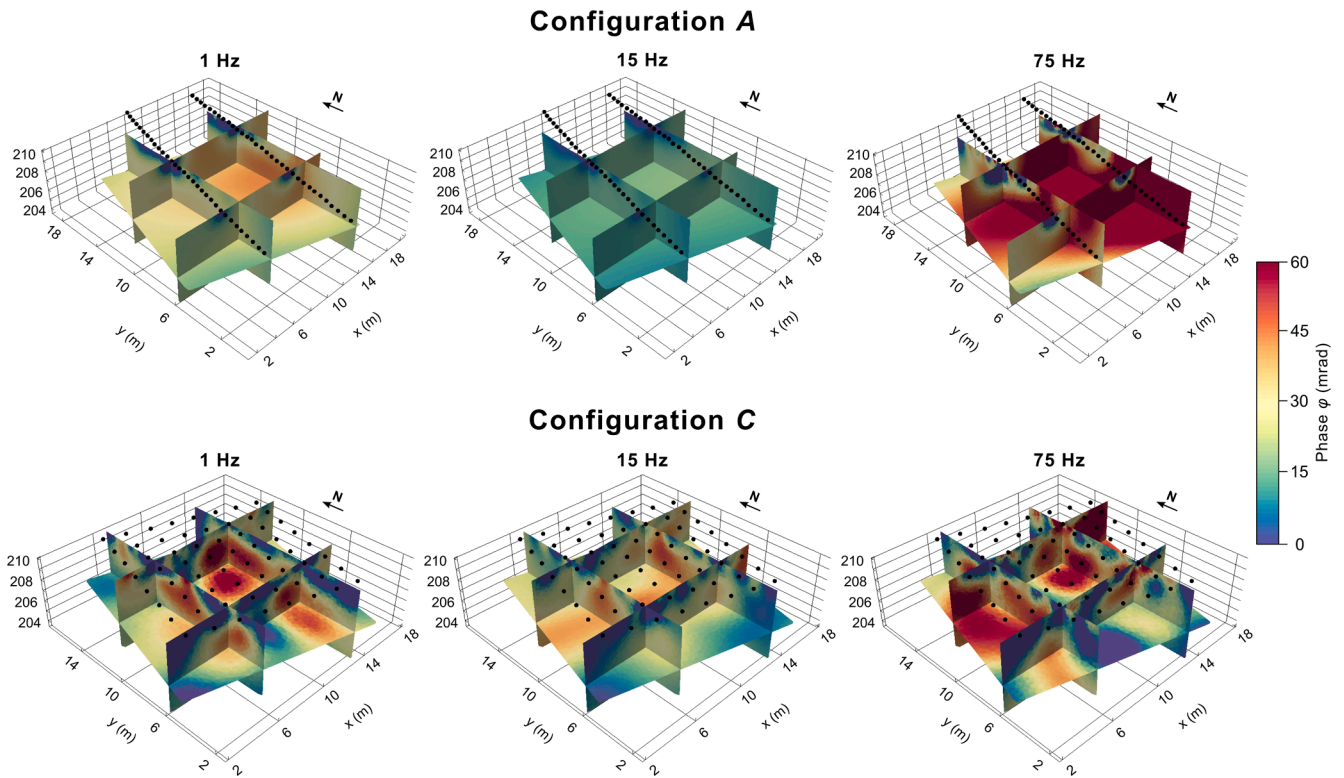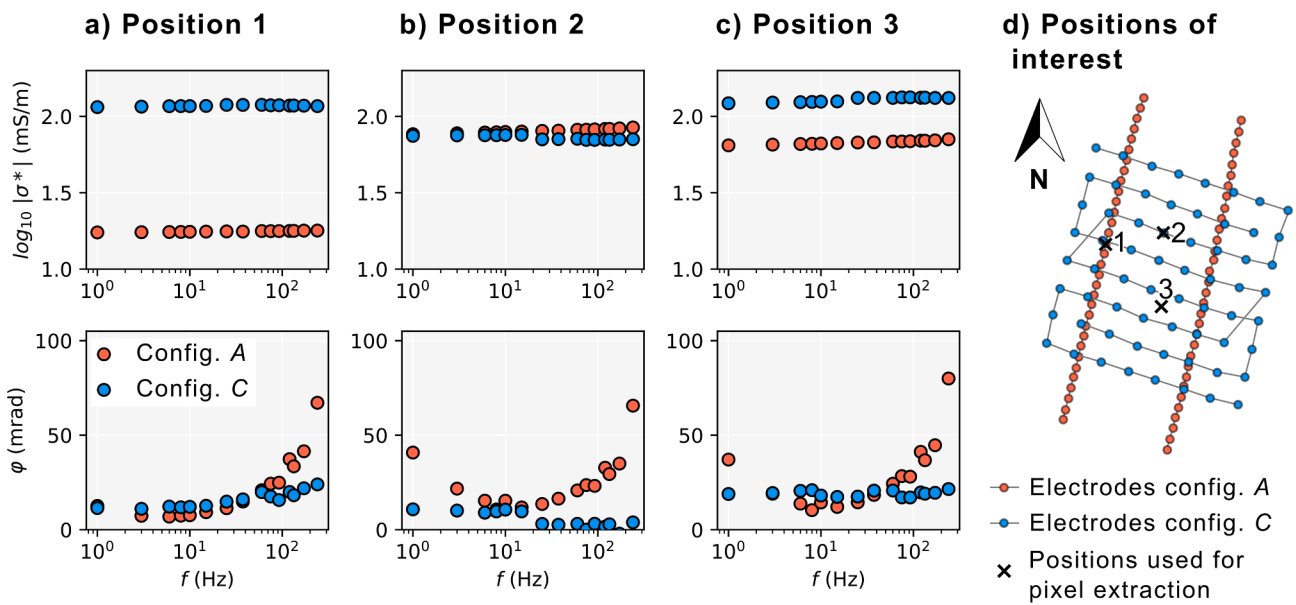

Configuration *C*

Fig. 6. Heferlbach landfill conductivity phase angle inversion results for SIP data collected at frequencies 1, 15 and 75 Hz, using configuration *A* (first line) and *C* (second line). Black dots represent the electrodes positions.

presence of TOC, as also observed for measurements in peatlands with high TOC (Katona et al., 2021). The increase at 75 Hz is likely due to the polarization of the fine materials that migrate together with leachates and accumulate at the bottom of the landfill (e.g., Bücker et al., 2019). As demonstrated by Flores-Orozco et al. (2020), the highly polarizable areas of the Heferlbach landfill are related to high concentration of organic waste and have been linked to TOC supporting our interpretation on the different polarization mechanisms underlying the response at

1 and 75 Hz. In this regard, 3D SIP might permit a better discrimination of polarizable anomalies due to biogeochemically active zones – associated to low frequencies (<10 Hz) – and fine-grained soil/waste with low TOC – related to a polarizable anomaly at high frequencies (>15 Hz).

Relaxation parameters can give further information about waste composition (see Gazoty et al., 2012). However, a quantitative estimation of relaxation parameters requires to resolve for the frequency-

Fig. 7. Conductivity magnitude (first row) and phase (second row) spectra (frequency range: 1–240 Hz) of the SIP inversion result for data collected at the Heferlbach landfill. Red symbols represent the results of configuration *A*, while blue symbols represent results of configuration *C*. The map (d) shows the position of the voxel values extracted with respect of the electrodes. Positions 1 and 2 are in a depth of 1 m below the ground level, while the depth of position 3 is 3 m.

dependence in the polarization effect at a broad frequency bandwidth. This might be particularly challenging for field scale surveys considering that different sources of error might distort the quality of the SIP data at high frequencies (>1 Hz) due to EM coupling adding further uncertainties in our inversion results (see Flores Orozco et al., 2018, 2021). To consider the influence of such error sources in the frequency-dependence of SIP surveys, we present in Fig. 7 voxel values extracted from the SIP inversion results (independently inverted with a heterogeneous starting model corresponding to the 0.5 Hz resistivity inverse model) of the Heferlbach landfill, in terms of $|\sigma^*|$ and φ. The results are presented for configuration B and C for three positions of interest (see location in d) in the frequency range between 1 and 240 Hz.

Fig. 7 shows large differences in the complex conductivity spectra (given in terms of the $|\sigma^*|$ and φ) between configuration A and C, revealing a clear frequency-dependence in the φ. For configuration A, φ spectra are relatively similar in all positions with one peak at the low frequencies (<0.5 Hz) and a second peak at the high frequencies (>240 Hz) revealing a lack in resolution of the heterogeneous electrical properties in the Heferlbach landfill. In contrast, spectra of configuration C show stronger spatial changes with peaks at different frequencies revealing that the frequency-dependence for real measurements might not be easily explained by a single Cole Cole model, as also discussed by Nordsiek and Weller (2008). At the field scale, we record responses of different materials with varying frequency-dependence, resulting in the superposition of more than one relaxation model (i.e., we require more than one Cole Cole model to describe our data). Additionally, distortions are evidenced in the recovered frequency-dependence of the φ related to the data quality at the Heferlbach site, which makes the estimation of relaxation parameters challenging. Further investigations are needed to enhance the quality of the SIP data at high frequencies and better recover the frequency-dependence of the electrical properties. For instance, SIP data collected with coaxial cables in MSW landfills need to be further investigated, aiming at reducing EM coupling associated to the cross-talk between the cables or inductive coupling effects. Nonetheless, our results demonstrate that the use of adequate 3D configurations is key to properly resolve for the spatial changes in the electrical properties.

3.5. The frequency-dependence and geometrical changes in 3D SIP imaging results for the CDW landfill Kappern

Building on the results discussed above, we only present SIP measurements in the Kappern landfill using configuration C with an electrode spacing of 5 m. The electrode separation was defined, as existing information of the landfill reports a thickness in the waste unit of ca. 10 m (although there is no information available about the waste composition). Fig. 8 shows the imaging results in terms of $|\sigma^*|$ and φ of the complex conductivity. The $|\sigma^*|$ results are only presented for 1 Hz because data collected (and inversions) at different frequencies reveal a minimal change; whereas φ images reveal a clear frequency-dependence and are therefore presented for 1, 15 and 75 Hz. The 1 Hz inverse model reveals an area of low $|\sigma^*|$ ($\log_{10} |\sigma^*| < 1.05$ mS/m) in the center of the electrodes from the surface to a depth that varies between 4.5 and 8.5 m (or deeper). This anomaly is associated with CDW waste mainly consisting of coarse-grained materials such as concrete, bricks and other masonry material (Austrian Environmental Agency, 2002). Underneath the waste unit, $|\sigma^*|$ increases ($\log_{10} |\sigma^*| > 1.1$ mS/m), apart from a small area in the center-south and in the center-north, each at a distance of 7.5 m from the center of the electrodes. The increase in the magnitude can be related to leachate migration (associated to high salinity and thus fluid conductivity) below the waste unit; however, it might also be indicative of a clay-rich unit corresponding to the low permeability layer underneath the landfill. No ground truth information is available about the landfill for this area, hindering the conclusive interpretation of the $|\sigma^*|$ results. In the waste unit, the φ response ($\varphi < 7.5$ mrad) is low for all frequencies investigated, and values are clearly lower to the MSW from the Heferlbach landfill discussed above. Hence, we can interpret that the area under study at the Kappern landfill is related to CDW, which is similar to the weak polarization of gravels and coarse materials (associated to low surface charge and area) in the frequency range between 1 and 75 Hz. The layer below characterized by higher φ values, might be indicative of a polarizable material, either due to organic materials leaking from the waste unit, or due to fine-grained material, which commonly shows a stronger polarization at high frequencies (75 Hz) (see Flores Orozco et al., 2022; Zisser et al., 2010). We note here that data above 15 Hz revealed larger data error (likely related to EM
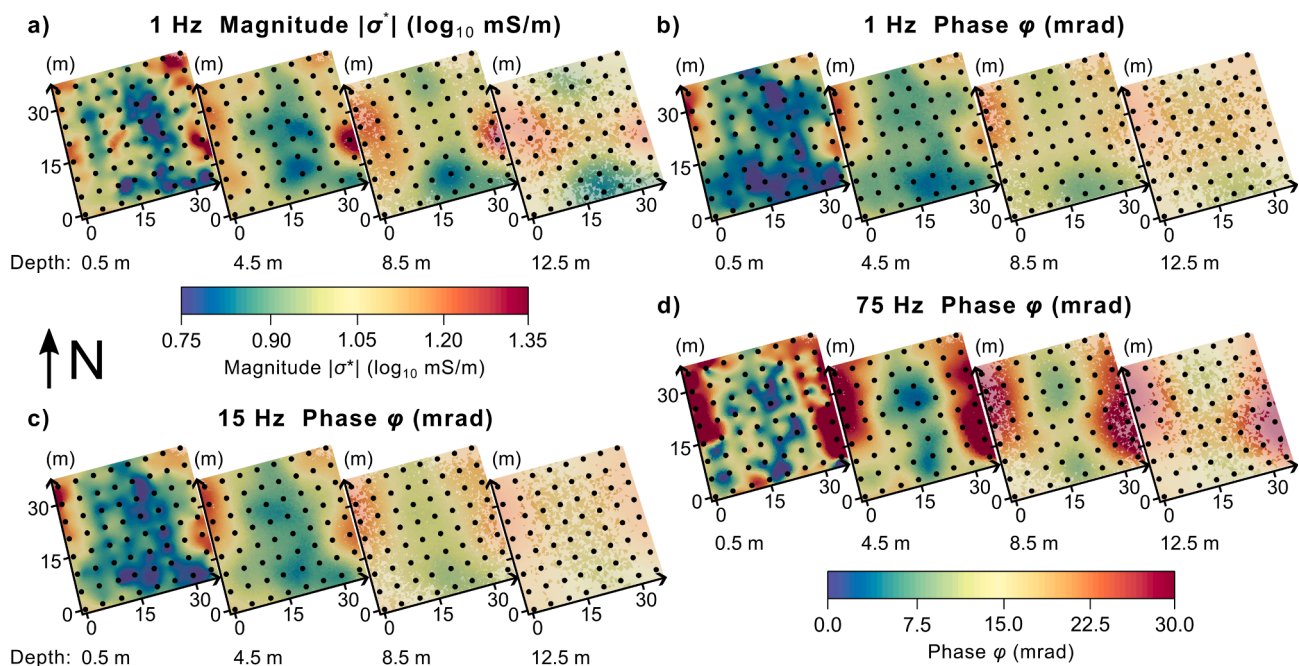

Fig. 8. Horizontal slices of the Kappern landfill inversion results of configuration C in terms of the conductivity magnitude (a) at 1 Hz and phase (b to d) at 1, 15 and 75 Hz. Black dots represent the electrodes positions.

coupling), especially for deep measurements, i.e., those with large separations between current and potential dipoles, associated to the lower signal-to-noise ratios (see Flores Orozco et al., 2018 for a discussion). Hence, imaging results above 15 Hz might be affected by a higher error than those at lower frequencies. Further SIP measurements should consider the use of coaxial cables to improve data quality at high frequencies as well as the deployment of larger electrode spacings.

3.6. Applying 3D configurations for spectral induced polarization investigations in landfills

Synthetic experiments of the spectral induced polarization method demonstrated that 3D configurations provide better results than 2D configurations at the spatial scale and for the frequency-dependence as they provide more accurate volume estimations of polarizable anomalies and more stable spectra of the frequency-dependence of the complex conductivity. Both, the spatial and spectral reconstruction quality are essential for investigations in landfills, where (1) the volume of waste units and (2) the waste type are primary fields of interest.

In landfills, waste units, which can be separated from the surrounding material by different electrical properties, are often highly heterogeneously distributed. Thus, the delineation of the geometry of waste units requires high resolution and high accuracy in all three dimensions. Field results of one MSW and one CDW landfill showed that such accuracy cannot be provided by 2D configurations leading to an incorrect quantification of the waste volumes related to the anomalies, as revealed in our synthetic experiment (c.f., Fig. 3). Using dipoles of different orientations, which were used in configuration *C* and *D*, allows high resolution of heterogeneous subsurface electrical conditions. Even closely spaced 2D electrode lines (separation between electrode lines smaller than the inline electrode separation) cannot provide the electrical properties of the subsurface in the same detail as real 3D configurations because of the single orientation in 2D measurements. Additionally, the field effort to build several closely spaced 2D electrode lines would exceed the field effort of building a real 3D configuration. Such observation is similar to the conclusions of Chambers et al. (2002) for resistivity surveys, who recommended to use not only data along parallel electrode lines with only one dipole orientation to create 3D resistivity models for heterogeneous subsurface electrical properties. Heterogeneous subsurface electrical conditions at the Heferlbach site are related to changes in waste composition, with high polarizable anomalies likely related to areas with high organic carbon and water content (Flores-Orozco et al., 2020), ideal conditions for the production of landfill gas. Although not investigated here, time-lapse 3D SIP measurements can also be used to evaluate the preferential flow paths for water within the landfill and to predict potential methane emissions.

Only a few commercial instruments are able to collect SIP data and the processing of such data requires larger efforts due to larger data sets (i.e., measurements for each frequency). Moreover, SIP measurements require careful field procedures to minimize EM coupling (Flores Orozco et al., 2021; Maierhofer et al., 2022). Nonetheless, the polarization response clearly provides further information for an adequate identification of waste composition, which can also be gained by means of time-domain or single-frequency IP data (Gazoty et al., 2012; Dahlin et al., 2010; Flores-Orozco et al., 2020). However, the reconstruction qualities of different 2D and 3D configurations presented in this study are not only valid for SIP surveys but also for time-domain and single-frequency IP surveys. Additionally, using single-frequency IP in landfill investigations can be misleading because the polarization of different waste materials can act at different frequencies related to different polarization mechanisms, as evidenced in the Heferlbach and Kappern landfills. Measurements collected at a single-frequency, or within a narrow frequency-bandwidth, may fail to retrieve the frequency at which the waste provides a strong response. Accordingly, the frequency-dependence of electrical properties can be used to discriminate between different waste types with different relaxation times, for instance

between metal deposits and organic material (Gazoty et al., 2012). Additionally, SIP results may permit the use of existing petrophysical relationships to quantify hydrogeological and textural properties, thus, allowing a quantitative interpretation of the SIP imaging results. Besides the collection of data in a broad frequency-bandwidth, the calculation of accurate relaxation parameters requires of stable inversion results for data collected at different frequencies. As evidenced by the synthetic experiments described above, the collection of data with real 3D configurations results in less noisy spectra which improves the reconstruction of the frequency-dependence of the complex conductivity, in particular of the chargeability parameter. Moreover, the use of the 3D inverted model at the lowest frequency results in improved consistency of the inversion results at different frequencies, as also demonstrated in our synthetic investigation. Hence, 3D configurations are critical on the field scale not only for the estimation of waste volume but also for the application of petrophysical models derived in the laboratory to determine the waste composition and to quantify textural, hydrogeological or biogeochemical properties of the subsurface.

4. Conclusions

In this study, we investigated the resolving capabilities of four different electrode configurations for 3D SIP surveys. In particular, we compared the reconstruction quality of several parallel 2D profiles inverted within a 3D algorithm and real 3D configurations with dipoles varying within rectangular and circular grids. Our investigations were based on the analysis of imaging results obtained in numerical and field SIP data sets.

Our numerical experiment demonstrates that configurations consisting of parallel 2D electrode lines with inline measurements were able to resolve the polarizable anomaly along the lines but failed to detect the anomaly between the lines due to a lack of sensitivity. In contrast, a 3D configuration with electrodes set in a quadratic mesh is able to resolve the geometry of the polarizable anomaly in the whole area of investigation; whereas a circular array with electrodes set in four concentric circles was not able to accurately resolve the geometry of the polarizable anomaly. The same conclusion can be achieved from measurements collected at the two landfills under investigation here. Real 3D configurations were able to delineate the 3D geometry of polarizable anomalies, which are related to changes in landfill geometry and waste composition and permit to estimate waste volumes accurately. However, the use of circular arrays reveals artifacts close to the surface. The use of electrodes placed on a 3D rectangular mesh also permits to easily change electrode spacing to gain information about different area and depth of investigation.

Our results demonstrate that 3D configurations provide more stable spectra (i.e., can better resolve the frequency-dependence) of the complex conductivity than 2D configurations. Spectra of 2D configurations are particularly noisy in areas between the electrode lines. Thus, relaxation parameters describing the frequency-dependence of the complex conductivity can be estimated more accurately by 3D configurations, which is essential to discriminate between different waste types in landfills.

Declaration of Competing Interest

The authors declare that they have no known competing financial interests or personal relationships that could have appeared to influence the work reported in this paper.

Data availability

Data will be made available on request. The orthophotos used in Fig. 2 were published by geoland.at under a CC BY 4.0 license.

Acknowledgement

Appendix A. Supplementary material

Supplementary data to this article can be found online at https://doi.org/10.1016/j.wasman.2023.07.006.

References

Abdulsamad, F., Revil, A., Soueid Ahmed, A., Coperey, A., Karaoulis, M., Nicaise, S., Peyras, L., 2019. Induced polarization tomography applied to the detection and the monitoring of leaks in embankments. Eng. Geol. 254, 89–101.

Aizebeokhai, A.P., Singh, V.S., 2013. Field evaluation of 3D geo-electrical resistivity imaging for environmental and engineering studies using parallel 2D profiles. Curr. Sci. 105 (4), 504–512.

Atekwana, E.A., Atekwana, E.A., 2010. Geophysical signatures of microbial activity at hydrocarbon contaminated sites: a review. Surv. Geophys. 31 (2), 247–283.

Auken, E., Doetsch, J., Fiandaca, G., Christiansen, A.V., Gazoty, A., Cahill, A.G., Jakobsen, R., 2014. Imaging subsurface migration of dissolved CO_2 in a shallow aquifer using 3-D time-lapse electrical resistivity tomography. J. Appl. Geophys. 101, 31–41.

Austrian Environmental Agency, 2002. Altlast O13 "Deponie Kappern". Beschreibung der Sicherungsmaßnahmen. Online (10.01.2023): https://www.altlasten.gv.at/atlas/verzeichnis/Oberoesterreich/Oberoesterreich-O13.html.

Austrian Environmental Agency, 2005, Altablagerung "Heferlbach". Gefährdungsabschätzung und Prioritätenklassifizierung. (§13 und §14 Altlastensanierungsgesetz). Online (10.01.2023): https://www.altlasten.gv.at/atlas/verzeichnis/Niederoesterreich/Niederoesterreich-N58.html.

Bentley, L.R., Gharibi, M., 2004. Two- and three-dimensional electrical resistivity imaging at a heterogeneous remediation site. Geophysics 69 (3), 674–680.

Bichet, V., Grisey, E., Aleya, L., 2016. Spatial characterization of leachate plume using electrical resistivity tomography in a landfill composed of old and new cells (Belfort, France). Eng. Geol. 211, 61–73.

Bièvre, G., Oxarango, L., Günther, T., Goutaland, D., Massardi, M., 2018. Improvement of 2D ERT measurements conducted along a small earth-filled dyke using 3D topographic data and 3D computation of geometric factors. J. Appl. Geophys. 153, 100–112.

Binley, A., Kemna, A., 2005. DC resistivity and induced polarization methods. In: Rubin, Y., Hubbard, S.S. (Eds.), Hydrogeophysics. Springer, pp. 129–156.

Binley, A., Slater, L.D., Fukes, M., Cassiani, G., 2005. Relationship between spectral induced polarization and hydraulic properties of saturated and unsaturated sandstone. Water Resour. Res. 41 (12).

Binley, A., Slater, L., 2020. Resistivity and Induced Polarization: Theory and Applications to the Near-Surface Earth. Cambridge University Press.

Blanchy, G., Saneiyan, S., Boyd, J., McLachlan, P., Binley, A., 2020. ResIPy, an intuitive open source software for complex geoelectrical inversion/modeling. Comput. Geosci. 137, 104423.

Bording, T.S., Fiandaca, G., Maurya, P.K., Auken, E., Christiansen, A.V., Tuxen, N., Klint, K.E.S., Larsen, T.H., 2019. Cross-borehole tomography with full-decay spectral time-domain induced polarization for mapping of potential contaminant flow-paths. J. Contam. Hydrol. 226, 103523.

Boyd, J., Chambers, J., Wilkinson, P., Peppa, M., Watlet, A., Kirkham, M., Jones, L., Swift, R., Meldrum, P., Uhlemann, S., Binley, A., 2021. A linked geomorphological and geophysical modelling methodology applied to an active landslide. Landslides 18 (8), 2689–2704.

Boyd, J., Blanchy, G., Saneiyan, S., McLachlan, P., Binley, A., 2019. 3D geoelectrical problems with ResiPy, an open source graphical user interface for geoelectrical data processing. Fast Times, 24, 85–92.

Brandstätter, C., Prantl, R., Fellner, J., 2020. Performance assessment of landfill in-situ aeration – a case study. Waste Manag. 101, 231–240.

Brunner, I., Friedel, S., Jacobs, F., Danckwardt, E., 1999. Investigation of a Tertiary maar structure using three-dimensional resistivity imaging. Geophys. J. Int. 136 (3), 771–780.

Bücker, M., Flores Orozco, A., Undorf, S., Kemna, A., 2019. On the role of stern- and diffuse-layer polarization mechanisms in porous media. J. Geophys. Res.: Solid Earth 124 (6), 5656–5677.

Buecker, M., Flores Orozco, A., Kemna, A., 2018. Electrochemical polarization around metallic particles — Part 1: the role of diffuse-layer and volume-diffusion relaxation. Geophysics 83 (4), E203–E217.

Cassiani, G., Kemna, A., Villa, A., Zimmermann, E., 2009. Spectral induced polarization for the characterization of free-phase hydrocarbon contamination of sediments with low clay content. Near Surf. Geophys. 7 (5-6), 547–562.

Chambers, J.E., Ogilvy, R.D., Kuras, O., Cripps, J.C., Meldrum, P.I., 2002. 3D electrical imaging of known targets at a controlled environmental test site. Environ. Geol. 41, 690–704.

Chambers, J.E., Kuras, O., Meldrum, P.I., Ogilvy, R.D., Hollands, J., 2006. Electrical resistivity tomography applied to geologic, hydrogeologic, and engineering investigations at a former waste-disposal site. Geophysics 71 (6), B231–B239.

Chambers, J.E., Wilkinson, P.B., Weller, A.L., Meldrum, P.I., Ogilvy, R.D., Caunt, S., 2007. Mineshaft imaging using surface and crosshole 3D electrical resistivity tomography: a case history from the East Pennine Coalfield, UK. J. Appl. Geophys. 62 (4), 324–337.

Chambers, J.E., Wilkinson, P.B., Wardrop, D., Hameed, A., Hill, I., Jeffrey, C., Loke, M. H., Meldrum, P.I., Kuras, O., Cave, M., Gunn, D.A., 2012. Bedrock detection beneath river terrace deposits using three-dimensional electrical resistivity tomography. Geomorphology 177–178, 17–25.

Chenq, Q., Chen, X., Tao, M., Binley, A., 2019. Characterization of karst structures using quasi-3D electrical resistivity tomography. Environ. Earth Sci. 78 (15).

Clément, R., Descloitres, M., Günther, T., Oxarango, L., Morra, C., Laurent, J.-P., Gourc, J.-P., 2010. Improvement of electrical resistivity tomography for leachate injection monitoring. Waste Manag. 30 (3), 452–464.

Dahlin, T., Bernstone, C., 1997. A roll-along technique for 3D resistivity data acquisition with multi-electrode arrays. In: Proceedings SAGEEP'97, Reno, Nevada, Vol. 2, pp. 927–935.

Dahlin, T., Bernstone, C., Loke, M. H., 2002a. A 3-D resistivity investigation of a contaminated site at Lernacken, Sweden. Geophysics 67(6), 1692–1700.

Dahlin, T., Leroux, V., Nissen, J., 2002b. Measuring techniques in induced polarisation imaging. J. Appl. Geophys. 50 (3), 279–298.

Dahlin, T., Leroux, V., 2012. Improvement in induced polarization data quality with multi-electrode systems by separating current and potential cables. Near Surf. Geophys. 10 (6), 545–565.

Dahlin, T., Rosqvist, H., Leroux, V., 2010. Resistivity-IP mapping for landfill applications. Near Surf. Geophys., first break 28 (8), 101–105.

De Carlo, L., Perri, M.T., Caputo, M.C., Deiana, R., Vurro, M., Cassiani, G., 2013. Characterization of a dismissed landfill via electrical resistivity tomography and mise-à-la-masse method. J. Appl. Geophys. 98, 1–10.

Di Maio, R., Fais, S., Ligas, P., Piegari, E., Raga, R., Cossu, R., 2018. 3D geophysical imaging for site-specific characterization plan of an old landfill. Waste Manag. 76, 629–642.

Flores Orozco, A., Williams, K.H., Long, P.E., Hubbard, S.S., Kemna, A., 2011. Using complex resistivity imaging to infer biogeochemical processes associated with bioremediation of an uranium-contaminated aquifer. J. Geophys. Res. 116 (G3).

Flores Orozco, A., Kemna, A., Oberdörster, C., Zschornack, L., Leven, C., Dietrich, P., Weiss, H., 2012a. Delineation of subsurface hydrocarbon contamination at a former hydrogenation plant using spectral induced polarization imaging. J. Contam. Hydrol. 136–137, 131–144.

Flores Orozco, A., Kemna, A., Zimmermann, E., 2012b. Data error quantification in spectral induced polarization imaging. Geophysics 77 (3), E227–E237.

Flores Orozco, A., Bücker, M., Steiner, M., Malet, J.-P., 2018. Complex-conductivity imaging for the understanding of landslide architecture. Eng. Geol. 243, 241–252.

Flores Orozco, A., Aigner, L., Gallistl, J., 2021. Investigation of cable effects in spectral induced polarization imaging at the field scale using multicore and coaxial cables. Geophysics 86 (1), E59–E75.

Flores Orozco, A., Steiner, M., Katona, T., Roser, N., Moser, C., Stumvoll, M.J., Glade, T., 2022. Application of induced polarization imaging across different scales to understand surface and groundwater flow at the Hofermuehle landslide. Catena 219, 106612.

Flores-Orozco, A., Gallistl, J., Steiner, M., Brandstätter, C., Fellner, J., 2020. Mapping biogeochemically active zones in landfills with induced polarization imaging: the Heferlbach landfill. Waste Manag. 107, 121–132.

Frid, V., Sharabi, I., Frid, M., Averbakh, A., 2017. Leachate detection via statistical analysis of electrical resistivity and induced polarization data at a waste disposal site (Northern Israel). Environ. Earth Sci. 76 (6).

Gallistl, J., Schwindt, D., Jochum, B., Aigner, L., Peresson, M., Flores Orozco, A., 2022. Quantification of soil textural and hydraulic properties in a complex conductivity imaging framework: results from the Wolfsegg slope. Front. Earth Sci. 10.

Gazoty, A., Fiandaca, G., Pedersen, J., Auken, E., Christiansen, A.V., 2012. Mapping of landfills using time-domain spectral induced polarization data: the Eskelund case study. Near Surf. Geophys. 10 (6), 575–586.

Geuzaine, C., Remacle, J.-F., 2009. Gmsh: A 3-D finite element mesh generator with built-in pre- and post-processing facilities. Int. J. Numer. Meth. Eng. 79 (11), 1309–1331.

Johansson, B., Jones, S., Dahlin, T., Flyhammar, P., 2007. Comparisons of 2D and 3D inverted resistivity data as well as of resistivity and IP surveys on a landfill. In: Proceedings of the 13th Near Surface Geophysics Conference, EAGE, Istanbul, Turkey, 3–5 September, P42.

Johnson, T.C., Versteeg, R.J., Ward, A., Day-Lewis, F.D., Revil, A., 2010. Improved hydrogeophysical characterization and monitoring through parallel modeling and inversion of time-domain resistivity and induced-polarization data. Geophysics 75 (4), WA27–WA41.

Johnson, T., Versteeg, R., Thomle, J., Hammond, G., Chen, X., Zachara, J., 2015. Four-dimensional electrical conductivity monitoring of stage-driven river water intrusion: accounting for water table effects using a transient mesh boundary and conditional inversion constraints. Water Resour. Res. 51 (8), 6177–6196.

Katona, T., Gilfedder, B.S., Frei, S., Buecker, M., Flores-Orozco, A., 2021. High-resolution induced polarization imaging of biogeochemical carbon turnover hotspots in a peatland. Biogeosciences 18, 4039–4058.

Kemna, A., 2000. Tomographic Inversion of Complex Resistivity: Theory and Application. Der Andere Verlag Osnabrück.

Kemna, A., Binley, A., Slater, L., 2004. Crosshole IP imaging for engineering and environmental applications. Geophysics 69 (1), 97–107.

Kemna, A., Binley, A., Cassiani, G., Niederleithinger, E., Revil, A., Slater, L., Williams, K. H., Orozco, A.F., Haegel, F.-H., Hördt, A., Kruschwitz, S., Leroux, V., Titov, K., Zimmermann, E., 2012. An overview of the spectral induced polarization method for near-surface applications. Near Surf. Geophys. 10 (6), 453–468.

LaBrecque, D., Birken, R., LaBrecque, D., 2021. Design of a Multi-Source Capable, Hybrid Cabled/Distributed ERT/IP data acquisition system. In: SEG Technical Program Expanded Abstracts, pp. 3063–3067.

LaBrecque, D., Miletto, M., Daily, W., Ramirez, A., Owen, E., 1996. The effect of noise on Occam's inversion of resistivity tomography data. Geophysics 61 (2), 538–548.

Leroux, V., Dahlin, T., Svensson, M., 2007. Dense resistivity and induced polarization profiling for a landfill restoration project at Härlöv, Southern Sweden. Waste Manage. Res. 25 (1), 49–60.

Leroy, P., Revil, A., Kemna, A., Cosenza, P., Ghorbani, A., 2008. Complex conductivity of water-saturated packs of glass beads. J. Colloid Interface Sci. 321 (1), 103–117.

Loke, M.H., Barker, R.D., 1996. Practical techniques for 3D resistivity surveys and data inversion. Geophys. Prospect. 44, 499–523.

Maierhofer, T., Hauck, C., Hilbich, C., Kemna, A., Flores-Orozco, A., 2022. Spectral induced polarization imaging to investigate an ice-rich mountain permafrost site in Switzerland. Cryosphere 16.

Maurya, P.K., Rønde, V.K., Fiandaca, G., Balbarini, N., Auken, E., Bjerg, P.L., Christiansen, A.V., 2017. Detailed landfill leachate plume mapping using 2D and 3D electrical resistivity tomography - with correlation to ionic strength measured in screens. J. Appl. Geophys. 138, 1–8.

McAnallen, L., Doherty, R., Donohue, S., Kirmizakis, P., Mendonça, C., 2018. Combined use of geophysical and geochemical methods to assess areas of active, degrading and restored blanket bog. Sci. Total Environ. 621, 762–771.

Nguyen, F., Ghose, R., Isunza Manrique, I., Robert, T., Dumont, G., 2018. Managing past landfills for future site development: a review of the contribution of geophysical methods. Paper read at Proceedings of the 4th International Symposium on Enhanced Landfill Mining.

Nimmer, R.E., Osiensky, J.L., Binley, A.M., Williams, B.C., 2008. Three-dimensional effects causing artifacts in two-dimensional, cross-borehole, electrical imaging. J. Hydrol. 359 (1-2), 59–70.

Nordsiek, S., Weller, A., 2008. A new approach to fitting induced-polarization spectra. Geophysics 73 (6), F235–F245.

Nyquist, J.E., Roth, M.J.S., 2005. Improved 3D pole-dipole resistivity surveys using radial measurement pairs. Geophys. Res. Lett. 32 (21).

Pelton, W.H., Ward, S.H., Hallof, P.G., Sill, W.R., Nelson, P.H., 1978. Mineral discrimination and removal of inductive coupling with multifrequency IP. Geophysics 43 (3), 588–609.

Revil, A., Coperey, A., Shao, Z., Florsch, N., Fabricius, I.L., Deng, Y., Delsman, J.R., Pauw, P.S., Karaoulis, M., de Louw, P.G.B., van Baaren, E.S., Dabekaussen, W., Menkovic, A., Gunnink, J.L., 2017. Complex conductivity of soils. Water Resour. Res. 53 (8), 7121–7147.

Revil, A., Florsch, N., 2010. Determination of permeability from spectral induced polarization in granular media. Geophys. J. Int. 181, 1480–1498.

Revil, A., Soueid Ahmed, A., Coperey, A., Ravanel, L., Sharma, R., Panwar, N., 2020. Induced polarization as a tool to characterize shallow landslides. J. Hydrol. 589, 125369.

Revil, A., Schmutz, M., Abdulsamad, F., Balde, A., Beck, C., Ghorbani, A., Hubbard, S.S., 2021. Field-scale estimation of soil properties from spectral induced polarization tomography. Geoderma 403, 115380.

Römhild, L., Fiandaca, G., Hu, L., Meyer, L., Bayer, P., 2022. Imaging hydraulic conductivity in near-surface aquifers by complementing cross-borehole induced polarization with hydraulic experiments. Adv. Water Resour. 170, 104322.

Ruecker, C., Guenther, T., Wagner, F.M., 2017. pyGIMLi: An open-source library for modelling and inversion in geophysics. Comput. Geosci. 109, 106–123.

Schurr, J.M., 1964. On the theory of the dielectric dispersion of spherical colloidal particles in electrolyte solution. J. Phys. Chem. 68, 2407–2413.

Slater, L., Binley, A.M., Daily, W., Johnson, R., 2000. Cross-hole electrical imaging of a controlled saline tracer injection. J. Appl. Geophys. 44 (2-3), 85–102.

Slater, L., Ntarlagiannis, D., Personna, Y.R., Hubbard, S., 2007. Pore-scale spectral induced polarization signatures associated with FeS biomineral transformations. Geophys. Res. Lett. 34 (21).

Slater, L.D., Ntarlagiannis, D., Day-Lewis, F.D., Mwakanyamale, K., Versteeg, R.J., Ward, A., Strickland, C., Johnson, C.D., Lane Jr., J.W., 2010. Use of Electrical Imaging and Distributed Temperature Sensing Methods to Characterize Surface Water–Groundwater Exchange Regulating Uranium Transport at the Hanford 300 Area. Water Resources Research, Washington, p. 46.

Soueid Ahmed, A., Revil, A., Byrdina, S., Coperey, A., Gailler, L., Grobbe, N., Viveiros, F., Silva, C., Jougnot, D., Ghorbani, A., Hogg, C., Kiyan, D., Rath, V., Heap, M.J., Grandis, H., Humaida, H., 2018. 3D electrical conductivity tomography of volcanoes. J. Volcanol. Geoth. Res. 356, 243–263.

Soupios, P., Papadopoulos, N., Papadopoulos, I., Kouli, M., Vallianatos, F., Sarris, A., Manios, T., 2007. Application of integrated methods in mapping waste disposal areas. Environ. Geol. 53 (3), 661–675.

Steiner, M., Katona, T., Fellner, J., Flores Orozco, A., 2022. Quantitative water content estimation in landfills through joint inversion of seismic refraction and electrical resistivity data considering surface conduction. Waste Manag. 169, 21–32.

Tsourlos, P., Papadopoulos, N., Yi, M.-J., Kim, J.-H., Tsokas, G., 2014. Comparison of measuring strategies for the 3-D electrical resistivity imaging of tumuli. J. Appl. Geophys. 101, 77–85.

Van Hoorde, M., Hermans, T., Dumont, G., Nguyen, F., 2017. 3D electrical resistivity tomography of karstified formations using cross-line measurements. Eng. Geol. 220, 123–132.

Vinegar, H.J., Waxman, M.H., 1984. Induced polarization of shaly sands. Geophysics 49 (8), 1267–1287.

Wainwright, H.M., Flores Orozco, A., Bücker, M., Dafflon, B., Chen, J., Hubbard, S.S., Williams, K.H., 2016. Hierarchical Bayesian method for mapping biogeochemical hot spots using induced polarization imaging. Water Resour. Res. 52 (1), 533–551.

Waxman, M.H., Smits, L.J.M., 1968. Electrical conductivities in oil-bearing shaly sands. Soc. Pet. Eng. J. 8, 107–122.

Weigand, M., Orozco, A.F., Kemna, A., 2017. Reconstruction quality of SIP parameters in multi-frequency complex resistivity imaging. Near Surf. Geophys. 15 (2), 187–199.

Weller, A., Slater, L., Nordsiek, S., Ntarlagiannis, D., 2010. On the estimation of specific surface per unit pore volume from induced polarization: a robust empirical relation fits multiple data sets. Geophysics 75 (4), WA105–WA112.

Weller, A., Slater, L., Binley, A., Nordsiek, S., Xu, S., 2015. Permeability prediction based on induced polarization: insights from measurements on sandstone and unconsolidated samples spanning a wide permeability range. Geophysics 80 (2), D161–D173.

Wilkinson, P., Chambers, J., Uhlemann, S., Meldrum, P., Smith, A., Dixon, N., Loke, M. H., 2016. Reconstruction of landslide movements by inversion of 4-D electrical resistivity tomography monitoring data. Geophys. Res. Lett. 43 (3), 1166–1174.

Wong, J., 1979. An electrochemical model of the induced-polarization phenomenon in disseminated sulfide ores. Geophysics 44 (7), 1245–1265.

Zisser, N., Kemna, A., Nover, G., 2010. Dependence of spectral-induced polarization response of sandstone on temperature and its relevance to permeability estimation. J. Geophys. Res. 115 (B9).